Renewable and Sustainable Energy Reviews 33 (2014) 701–718

Contents lists available at ScienceDirect

Renewable and Sustainable Energy Reviews

journal homepage: www.elsevier.com/locate/rser

Challenges in the electrochemical modelling of solid oxide fuel and electrolyser cells

M. García-Camprubí, S. Izquierdo, N. Fueyo *

Fluid Mechanics Group (University of Zaragoza) and LIFTEC (CSIC), María de Luna 3, 50018 Zaragoza, Spain

ARTICLE INFO

Article history:
Received 19 March 2013
Received in revised form
17 February 2014
Accepted 22 February 2014
Available online 15 March 2014

Keywords:
SOFC
SOEC
Electrochemical fitting
Exchange current density
Transfer coefficient
Modelling

ABSTRACT

Computational fluid dynamics (CFD) tools for the modelling of solid oxide fuel cells (SOFC), solid oxide electrolyser cells (SOEC) or solid oxide regenerative fuel cells (SORFC) nearly always require a fitting process prior to its application for cell design or optimisation purposes. In this fitting, a set of experimental data is used to guess the value of those parameters of the model that cannot be either modelled or measured experimentally. This is crucially the case of the charge transfer coefficients ($\alpha_{b,a}, \alpha_{f,a}, \alpha_{b,c}, \alpha_{f,c}$) and the exchange current densities ($i_{o,a}, i_{o,c}$) in the Butler–Volmer equation (*i.e.* electrochemical model).

The fitting of the electrochemical parameters in the SOFC, SOEC and SORFC modelling literature is reviewed in this work. It is found that this process is only vaguely discussed, if mentioned at all. In the authors' opinion, this practice contributes with uncertainty rather than guidance, since this fitting process is of utmost significance for making reliable quantitative predictions.

In this work, we further introduce a comprehensive model for the simulation of solid oxide regenerative fuel cells, *i.e.* a model that simulates, without any ad hoc adjustments or tuning, both the SOFC and SOEC modes. We also describe in detail how the electrochemical parameters are fitted, and discuss the applicability of the values commonly used in the literature for these fitted parameters and their proper validation. Finally, the validity of the proposed model and fitted parameters is shown by comparison of the numerical results with experimental data.

© 2014 Elsevier Ltd. All rights reserved.

Contents

* Corresponding author. Tel.: +34 976762153; fax: +34 976761882.
E-mail address: Norberto.Fueyo@unizar.es (N. Fueyo).

http://dx.doi.org/10.1016/j.rser.2014.02.034
1364-0321 © 2014 Elsevier Ltd. All rights reserved.

1. Introduction

Hydrogen has been identified as a promising energy carrier: it can be cleanly produced in a water electrolyser driven by renewable energy; it may be then stored or transported, and eventually converted back into water and electricity in a fuel cell. A Solid Oxide Regenerative Fuel Cell (SORFC) is an electrochemical device that allows both operating modes, *i.e.* it can operate reversibly either as a fuel cell or as an electrolyser.

An SORFC operating as a solid oxide fuel cell (SOFC) generates electricity, heat and water from hydrogen and oxygen. An SORFC operating as a solid oxide electrolyser cell (SOEC) produces hydrogen and oxygen when water, heat and electricity are supplied.

The reversibility of the solid oxide cells was first proved in the 1990s for both tubular and planar geometries [3–5]; however, research in this field subsided due to the low prices of fossil fuels. In recent years environmental, economic and geopolitical concerns over fossil fuels have rekindled the interest in this technology. This is evinced by the ongoing research work for both planar [6–8] and microtubular solid oxide regenerative fuel cells [9,10].

Numerical modelling is a primary tool to understand, and optimise, the operation of solid oxide cells, either in fuel-cell or electrolyser mode. The modelling of *either* SOFCs *or* SOECs has been the subject of many papers [11–19]. Often such models use computational fluid dynamics (CFD) to simulate all the relevant mass, heat and charge transfer processes. Wang et al. [1] present an overview of the several modelling alternatives, including: physical models (by which they mean those that represent, mathematically, the underlying physics, be it in zero, one, multiple spatial dimensions); equivalent circuit models (based on electrochemical impedance spectroscopy, or EIS, measurements); and "gray-" and "black-box" models (such as Artificial Neural Networks and neuro-fuzzy systems). The review paper by Hajimolana et al. [2] is a systematic inventory of the main submodels proposed for the mathematical representation of all the relevant physical processes in the several spatial domains (gas channels, electrodes, electrolyte, interconnects).

References reporting the modelling of *both* SOFC *and* SOEC operating modes (*i.e.* SORFC) with a *single* CFD model that works satisfactorily in both situations are very scarce. To the authors' knowledge only Jin and Xue [20] have presented a validated numerical tool for the simulation of SORFCs. (Ni et al. [21,22] address the modelling and validation of a reversible solid oxide fuel cell, but in fact they only report the SOEC behaviour.) If properly formulated, a CFD model for either SOFCs or SOECs should produce suitable results in the other regime without any modification to the laws (submodels) for the underlying fundamental physics. However, this is not the case for most models, as shown below. This paper reviews the challenges posed by the development of such a unified model, and how to overcome them.

Any comprehensive SOFC, SOEC or SORFC model relies to a certain extent on data fitting to find values for some of the physical parameters, as it is the case of the charge transfer coefficients ($\alpha_{b,a}, \alpha_{f,a}, \alpha_{b,c}, \alpha_{f,c}$) and the exchange current densities ($i_{o,a}, i_{o,c}$) in the electrochemical model. This fitting, when properly resorted to, is the consequence of the incomplete knowledge of the underlying physical phenomena, or of the excessive complexity of such phenomena for them to be accommodated within a fluid-flow model. The disparity of spatial scales between these phenomena and the device to be simulated is often one of the sources of this complexity.

However, often this fitting process is only vaguely discussed in the literature. Table 1 summarises the common practices in the SOFC, SOEC and SORFC modelling literature to evaluate the

Table 1
Review of the evaluation of the electrochemical parameters in SOFC, SOEC and SORFC modelling literature.$f(\odot)$ means "calculated as a function of $\odot$".

Model	Fitting	$\alpha_{b,a}/\alpha_{f,a}$	$\alpha_{b,c}/\alpha_{f,c}$	$i_{o,a}/i_{o,c}$	Value source
SOFC					
[25]	No	0.5/0.5	0.5/0.5	f(T)	From [56]/ guessed
[57]	No	0.5/0.5	0.5/0.5	5300/2000 A m^{-2}	From [58]
[50]	No	0.5/0.5	0.5/0.5	5300/2300 A m^{-2}	Not justified
[12]	No	0.5/0.5	0.5/0.5	7460/10090 A m^{-2}	Not justified
[59]	No	0.5/0.5	0.5/0.5	5300/2000 A m^{-2}	From [57]
[60,15]	Yes	0.5/0.5	0.5/0.5	Both f(T, species)	Fitting
[16]	Yes	0.5/0.5	0.5/0.5	Both f(T, species)	Fitting
[45]	Yes	1.5/0.5	0.75/0.25	Both f(T, species)	Fitting
[28]	Yes	2/1 [23]	1.5/0.5 [24]	Both f(T, species)	Fitting
SOEC					
[61,62]	No	0.5/0.5	0.5/0.5	Both from [25]	SOFC
[29]	Yes	0.5/0.5	0.5/0.5	Kinetics/fitted	Poor fitting
[63]	No	–	–	–	Not mentioned
[21,17,26]	No	0.5/0.5	0.5/0.5	2000/5300 A m^{-2}	From [57]
[22]	Yes	0.5/0.5	0.5/0.5	200 A m^{-2}/	Not mentioned
[19]	Yes	0.5/0.5	0.5/0.5	Fitted	Poor agreement
[51]	No	0.5/0.5	0.5/0.5	Both f(T, species)	Literature
SORFC					
[20]	Yes	0.5/0.5	0.5/0.5	1/0.1 A m^{-2}	Fitting

Nomenclature

a	exponent, Eq. (52), dimensionless
A	constant in the ionic conductivity equation, Eq. (A.19), $A\,V^{-1}\,m^{-1}$
$a_{1\alpha}$	JANAF constant for species α, dimensionless
$a_{2\alpha}$	JANAF constant for species α, K^{-1}
$a_{3\alpha}$	JANAF constant for species α, K^{-2}
$a_{4\alpha}$	JANAF constant for species α, K^{-3}
$a_{5\alpha}$	JANAF constant for species α, K^{-4}
b	exponent, Eq. (52), dimensionless
B	constant in the ionic conductivity equation, Eq. (A.19), K
B_0	porous-medium permeability-coefficient, m^2
c	exponent, Eq. (53), dimensionless
c_α	molar density of species α, $kmol\,m^{-3}$
C_p	specific heat at constant pressure of the fluid, $m^2\,s^{-2}\,K^{-1}$
$C_{p\alpha}$	specific heat at constant pressure of species α, $m^2\,s^{-2}\,K^{-1}$
d_p	mean pore diameter, m
$\mathcal{D}_{\alpha\beta}$	ordinary diffusion coefficient of species α in species β, $m^2\,s^{-1}$
$\mathcal{D}_{\alpha m}$	ordinary diffusion coefficient of species α in a multicomponent mixture, $m^2\,s^{-1}$
$\mathcal{D}_{K\alpha}$	Knudsen-diffusion coefficient of species α, $m^2\,s^{-1}$
E_{act}	activation energy, $kg\,m^2\,s^{-2}\,kmol^{-1}$
E_b	black-body emissive power, $kg\,s^{-3}$
E	electric potential difference, V
E^o	standard electric-potential difference, V
F	Faraday's constant, $A\,s\,kmol^{-1}$
F_{i-j}	view factor between the i-th and the j-th surface elements, dimensionless
h	sensible enthalpy of the fluid, $m^2\,s^{-2}$
h_α	sensible enthalpy of species α, $m^2\,s^{-2}$
H_o	external irradiation, $kg\,s^{-3}$
i	current density magnitude, $A\,m^{-2}$
$\vec{i}$	current density, $A\,m^{-2}$
i_o	exchange current density, $A\,m^{-2}$
$\vec{j}_\alpha$	mass diffusion-flux of species α relative to the mass-average velocity, $kg\,m^2\,s^{-1}$
$\langle \vec{j}_\alpha \rangle$	superficial mass diffusion-flux of species α through a porous media, $kg\,m^2\,s^{-1}$
k_B	Boltzmann constant, $kg\,m^2\,s^{-2}\,K^{-1}$
n	number of electrons released during the ionisation process of one fuel molecule, dimensionless
$\vec{N}_\alpha$	total molar flux of species α, $kmol\,m^{-2}\,s^{-1}$
p	pressure, $kg\,m^{-1}\,s^{-2}$
p_α	partial pressure of species α, $kg\,m^{-1}\,s^{-2}$
$\vec{q}$	energy flux, $kg\,s^{-3}$
Q	volumetric heat sources/sinks, Joule heat, $kg\,m^{-1}\,s^{-3}$
r	length from the i-th to the j-th surface elements, m
R	ideal gas constant, $kg\,m^2\,s^{-2}\,kmol^{-1}\,K^{-1}$
S_{y_α}	mass source or sink of species α, $kg\,m^3\,s^{-1}$
$S_{o\lambda\alpha}$	Sutherland-law parameter for species α, K
$S_{o\mu\alpha}$	Sutherland-law parameter for species α, K
S_{x_α}	molar source or sink of species α, $kmol\,m^3\,s^{-1}$
t	time, s
T	temperature, K
$\mathbb{T}$	parameter defined in Eq. (A.7), dimensionless
$T_{o\lambda\alpha}$	Sutherland-law parameter for species α, K
$T_{o\mu\alpha}$	Sutherland-law parameter for species α, K
$\vec{v}$	fluid mass-averaged velocity, $m\,s^{-1}$
$\langle \vec{v} \rangle$	superficial permeation velocity, $m\,s^{-1}$
V	voltage, V
W	molecular weight of the fluid, $kg\,kmol^{-1}$
W_α	molecular weight of species α, $kg\,kmol^{-1}$
x_α	molar fraction of species α, dimensionless
y_α	mass fraction of species α, dimensionless

Greek letters

α	species, dimensionless
α_b	backward transfer coefficient, dimensionless
α_f	forward transfer coefficient, dimensionless
γ	pre-exponential coefficient, $A\,m^{-2}$
Γ_α	dusty-gas model parameter, Eq. (12), $m^2\,s^{-1}$
Γ^*_α	dusty-gas model parameter, Eq. (12), $kg^{-1}\,s^1\,kmol$
ΔH_r	specific enthalpy of reaction, $kg\,m^2\,s^{-2}\,kmol^{-1}$
ε	porosity of the porous medium, dimensionless
ε_α	characteristic energy of species α , $kg\,m^2\,s^{-2}$
η_{act}	activation overpotential, V
η_{con}	concentration overpotential, V
η_{ohm}	Ohmic overpotential, V
θ	angle,
λ	thermal conductivity of the fluid, $kg\,m\,s^{-3}\,K^{-1}$
λ_α	thermal conductivity of species α, $kg\,m\,s^{-3}\,K^{-1}$
$\lambda_{o\alpha}$	Sutherland-law parameter for species α, $kg\,m\,s^{-3}\,K^{-1}$
μ	fluid viscosity, $kg\,m^{-1}\,s^{-1}$
μ_α	viscosity of species α, $kg\,m^{-1}\,s^{-1}$
$\mu_{o\alpha}$	Sutherland-law parameter for species α, $kg\,m^{-1}\,s^{-1}$
ν	number of occurrences of the rate determining step in an overall reaction, dimensionless
ξ	surface emissivity, dimensionless
ρ	mass density of the fluid, $kg\,m^{-3}$
$\tilde{\rho}$	charge density, $C\,m^{-3}$
$\tilde{\sigma}$	ionic conductivity, $A\,V^{-1}\,m^{-1}$
σ_α	characteristic length of species α, Å
$\sigma_{\alpha\beta}$	average collision diameter of species α and β, Å
σ_{sb}	Stefan–Boltzmann constant, $kg\,s^{-3}\,K^{-4}$
τ	tortuosity factor of the porous medium, dimensionless
$\vec{\upsilon}^{\,p}$	dusty-gas model parameter, Eq. (13), $m\,s^{-1}$
$\vec{\upsilon}^{\,p*}_\alpha$	dusty-gas model parameter, Eq. (13), $kg^{-1}\,m^{-1}\,s^1\,kmol$
$\vec{\upsilon}^{\,N}$	dusty-gas model parameter, Eq. (14), $m\,s^{-1}$
$\vec{\upsilon}^{\,N*}_\alpha$	dusty-gas model parameter, Eq. (14), $kg^{-1}\,m^{-1}\,s^1\,kmol$
ϕ	electric potential, V
ϕ_a	electric potential of the electric-conducting phase of the fuel electrode, V
ϕ_c	electric potential of the electric-conducting phase of the air electrode, V
ϕ_e	electric potential of the ion-conducting phase of the electrolyte, V
ϕ^*_e	effective electric potential of the ion-conducting phase of the electrolyte, V
$\Phi_{\alpha\beta}$	semi-empirical correlation parameter, Eq. (A.12), dimensionless
ω	heat of reaction, $kg\,m^{-1}\,s^{-3}$
Ω_D	collision integral, dimensionless

Subscripts

a	fuel electrode
b	bulk, feeding mixture concentration

c	air electrode
e	electrolyte
eq	equilibrium
f	fluid
i	isothermal-surface index
ia	interconnect/fuel–electrode interface
ic	interconnect/air–electrode interface
$irrev$	irreversible
j	isothermal-surface index
oc	open circuit
r	generic reaction wall, *i.e.* electrode–electrolyte interface
ra	anode reaction wall, *i.e.* anode–electrolyte interface
rc	cathode reaction wall, *i.e.* cathode–electrolyte interface
rad	radiation
ref	reference value
rev	reversible
s	solid
$SOEC$	at SOEC mode
$SOFC$	at SOFC mode

Superscripts

eff	effective value in the porous media

electrochemical parameters. It is widely assumed that the charge transfer coefficients are equal to 0.5, what would imply a single step, single electron reaction. Theoretically, it is clear that this assumption does not apply to the hydrogen reduction/oxidation reaction. Experimentally, there are interesting works refuting this hypothesis [23,24]. Numerically, there is also an interesting contribution of Grondin et al. [19] stating that Butler–Volmer equation together with the single step, single electron hypothesis does not permit relevant computing predictions of SOEC polarisation curves. However, this assumption is still used as it is simple and provides (apparently) good fitting to experimental data. In this work, we show that this assumption fails if the model is properly validated and that more accurate values can be found by means of a thorough, careful fitting process.

Once the electrochemical reaction is assumed as a single step, single electron one, the exchange current densities are the remaining unknowns of the model. How these are found and reported in the published literature deserves some close scrutiny. As shown in Table 1, some papers in the literature do not mention these values. Sometimes, when no experimental data is found these values are guessed without any further validation [25]. Some authors take constant values from published experimental works, even if the operating conditions or materials of the experimental cell do not match those of the cell being modelled [21,26]. For instance, Ni et al. [26] assume that the exchange current density of the carbon dioxide electrolysis is that of the water electrolysis. Ni et al. [21] validate the numerical data with the experimental data of Momma et al. [27], at first sight this validation would indicate that taking constant values from the literature may lead to reasonable fitting with experimental data. However, close examination of the experimental data used [27] reveals that only the linear range of the experimental characteristic curve is used ($i \in (0, 5000)$ A m^{-2}), avoiding the comparison with the experimental data at high current densities where the experimental trend is not linear anymore. Table 1 also shows that the value of the exchange current densities is estimated, in other works, to fit the numerical results to an experimental data set. For example, in [20] a constant value for both exchange current densities is guessed to fit the experimental data, neglecting its dependence on temperature and species concentration; the resulting values are unusually small ($1, 0.1$ A m^{-2}). This is also done in [22] for one exchange current density, but the authors do not indicate whether it is the cathodic or the anodic one. In the SOFC literature, it is a common practice to use experimental correlations that express the exchange current densities as a function of the temperature and species distribution at the electrodes, *e.g.* [28]. These are generally Arrhenius type expressions, the pre-exponential factors of which are the fitted parameters. In the SOEC literature this kind of correlation is used in [29] leading to a very poor agreement.

From the above review, the authors conclude that the evaluation of the electrochemical parameters is, in general, not properly justified. In our opinion, this not only greatly diminishes the usefulness of modelling as a design tool, but also contributes with uncertainty rather than guidance when published in the literature.

In the present work we introduce a comprehensive model for the simulation of an SORFC, together with a detailed description of how the electrochemical parameters are fitted. The validity of the proposed model and fitted parameters is also shown by comparison of the numerical results with experimental data for a microtubular SORFC [10].

The model presented caters for the following phenomena: (a) mass transport through channels; (b) momentum transport through channels and porous solids; (c) multispecies mass transfer through porous media (convection, ordinary diffusion, Knudsen diffusion); (d) heat transfer in gases, porous media and solids by conduction, convection and radiation; (e) charge transport through an impervious solid; and (f) reversible electrochemistry. The model has been implemented in OpenFOAM-1.5-dev [30], an open-source CFD platform based on the finite-volume method. The full mathematical model and the relevant features of the numerical method are thoroughly described in Sections 2 and 3 respectively. The model can be regarded as a compendium of the most appropriate submodels found in the literature for the task; and the full description of this comprehensive model in this paper should enable its implementation in any code by any interested researcher.

The model is validated using experimental data presented in Section 4. The unavoidable fitting process is next described in Section 5. It reveals that some common simplifications used in the SOFC and SOEC modelling literature (see Table 1) might be inappropriate. Our findings highlight the often-ignored relevance of this fitting process for obtaining a predictive tool that can be used reliably across the range of SOFC, SOEC and SORFC designs.

Finally in Section 6 our numerical results are compared with experimental data to validate the model. Not only the numerical and experimental characteristic $\bar{i}$–V curves agree well, but so do the magnitudes of other variables that depend on the fitted parameters, such as the exchange current density and the activation overpotential.

2. Mathematical model

In this section the mathematical model that describes the operating principles of an SORFC is presented. The model is an extension of one developed previously for SOFC simulation [16,31], the new features being: (i) a new multidimensional charge-transfer model for the electrolyte; (ii) an improved formulation of the calculation of heat sources and sinks; (iii) the extension of the electrochemical model to SOEC conditions.

The operating principle of a solid oxide regenerative fuel cell, both in SOFC and SOEC modes, involves a complex network of interdependent physical phenomena within the several SORFC components. The governing equations that describe a given physical phenomenon may change from one component to another because of the components' differing nature, *e.g.* porous media, gas channels or impervious solids. To describe each phenomenon with the appropriate equations, the mathematical model has been split into a set of submodels, namely: (i) channel; (ii) electrode; and (iii) electrolyte submodels. Two additional submodels account for the radiative heat transfer and the electrochemistry; these operate at the interface between some of the components (respectively channel–electrode and electrode–electrolyte).

2.1. Channel model

The SORFC channels are ducts along which the reactant mixtures are driven from the SORFC inlet to the electrodes. The byproducts of the electrochemical reactions exit the electrode and join the unconverted reactants in the channel, where they are evacuated to the SORFC outlet. The channel model accounts for the phenomena summarised in Table 2 and described below.

The differential form of the continuity equation is

$$\frac{\partial \rho}{\partial t}+\nabla\cdot(\rho\vec{v})=0 \tag{1}$$

where $\vec{v}$ is the fluid velocity and ρ is the fluid density, given by the ideal gas law:

$$\rho=\frac{pW}{RT} \tag{2}$$

where p is the pressure, W the mixture molecular weight, T the temperature and R the ideal gas constant.

The momentum-conservation equation for a Newtonian fluid with negligible bulk viscosity ($\mu_V\approx 0$), with negligible body forces, is (in vector form)

$$\frac{\partial(\rho\vec{v})}{\partial t}+\nabla\cdot(\rho\vec{v}\vec{v})-\nabla\cdot(\mu\nabla\vec{v})=\nabla\cdot\left[\mu(\nabla\vec{v})^{\mathsf{T}}-\frac{2}{3}\mu\,\mathrm{tr}[(\nabla\vec{v})^{\mathsf{T}}]\vec{\vec{I}}\right]-\nabla p \tag{3}$$

where μ is the dynamic viscosity of the fluid (see Appendix A.1).

The differential form of the equation for the conservation of chemical species α in the channel is

$$\frac{\partial(\rho y_\alpha)}{\partial t}+\nabla\cdot(\rho y_\alpha\vec{v})+\nabla\cdot\vec{j}_\alpha=S_{y_\alpha} \tag{4}$$

where y_α is the mass fraction of species α, $\vec{j}_\alpha$ is the mass diffusion-flux of species α relative to the mass-average velocity, and S_{y_α} stands for the volumetric sources or sinks.

Table 2
Summary of the main features of the mathematical submodels.

Submodel	Phenomena	State/constitutive equations
Channel	Mass transport	Ideal gas
	Momentum transport	Newtonian fluid
	Species transport	Consistent diffusion
	Energy transport	Fourier multicomponent
Electrode	Mass transport	Ideal gas
	Momentum transport	Darcy
	Species transport	Dusty-gas
	Energy transport	Fourier multicomponent
Electrolyte	Charge transport	Ohm
	Energy transport	Fourier
Radiation	Surface-to-surface	View-factor method
Electrochemical	Redox	Nernst, Butler–Volmer

We model $\vec{j}_\alpha$ according to the consistent effective binary diffusion method [32]:

$$\vec{j}_\alpha=-\rho\mathcal{D}_{\alpha m}\nabla y_\alpha+\rho y_\alpha\sum_{\forall\beta}(\mathcal{D}_{\beta m}\nabla y_\beta) \tag{5}$$

where $\mathcal{D}_{\alpha m}$ is the diffusion coefficient of species α in a multi-component gas mixture (see Appendix A.2). This formulation ensures that the diffusive fluxes relative to averaged fluid velocity properly add up to zero. It thus combines the simplicity of the effective binary diffusion approach with flux consistency.

From Eqs. (4) and (5), the conservation equation of a chemical species α in the SORFC channel is

$$\frac{\partial(\rho y_\alpha)}{\partial t}+\nabla\cdot(\rho y_\alpha\vec{v})-\nabla\cdot(\rho\mathcal{D}_{\alpha m}\nabla y_\alpha)+\nabla\cdot\left[\rho y_\alpha\sum_{\forall\beta}(\mathcal{D}_{\beta m}\nabla y_\beta)\right]=S_{y_\alpha} \tag{6}$$

The conservation of energy in the system is accounted for through the following equation for the sensible enthalpy:

$$\rho C_p\frac{\partial T}{\partial t}+\nabla\cdot(\rho C_p\vec{v}T)-\nabla\cdot(\lambda\nabla T)=-\sum_{\forall\alpha}(y_\alpha h_\alpha)\frac{\partial\rho}{\partial t}+T\nabla\cdot(C_p\rho\vec{v})-\nabla\cdot\left[\sum_{\forall\alpha}(\vec{j}_\alpha h_\alpha)\right] \tag{7}$$

where C_p is the fluid specific heat at constant pressure (see Appendix A.5), λ is the thermal conductivity of the fluid (see Appendix A.4), and h_α is the sensible enthalpy of species α (see Appendix A.6).

In Eq. (7) the following assumptions and provisions have been made [16]: (i) the sensible enthalpy is defined as $dh=C_p dT$; (ii) the specific heat at constant pressure depends on temperature $C_p=f(T)$ (see Appendix A.5); (iii) the diffusion of heat is due to both heat conduction (Fourier's law) and species mass diffusion; (iv) the power delivered to the fluid by body forces is negligible; (v) viscous dissipation of energy can be neglected; (vi) large pressure differences in the system are not expected; (vii) the reaction heat-release within the channel is null since the reaction sites are located in the electrodes; and (viii) radiation is from surface to surface, and hence there are no volumetric sources of radiative heat in the channels [33,34].

2.2. The electrode model

The electrode model accounts for the momentum, mass, species and heat transport within the SORFC electrodes; both anode and cathode are porous ceramics that are assumed to be homogeneous and isotropic.

The conservation equation for the species α in a porous medium, *i.e.* the counterpart in the electrode to Eq. (4) in the channel, is

$$\frac{\partial(\varepsilon\rho y_\alpha)}{\partial t}+\nabla\cdot(\rho y_\alpha\langle\vec{v}\rangle)+\nabla\cdot\langle\vec{j}_\alpha\rangle=S_{y\alpha} \tag{8}$$

where $\langle\vec{v}\rangle$ is the fluid permeation velocity through the electrode (or superficial velocity) and $\langle\vec{j}_\alpha\rangle=\varepsilon\vec{j}_\alpha$ represents the superficial combined diffusion flux (ordinary and Knudsen) through the porous medium.

The dusty gas model (DGM) is the most convenient approach to model such a species transfer, as reported in [35,36]. It is worth noting, though, that the theoretical basis of the DGM [37] was criticised by Kerkhof [38,39], who as an alternative proposed the binary-friction model (BFM). However, the BFM does not improve the DGM results [38] and both models showed similar agreements and discrepancies with experimental data. The DGM is thus used in this work; its general form is as follows [37]:

$$-\frac{1}{RT}\nabla p_\alpha=\sum_{\beta\neq\alpha}\frac{x_\beta\vec{N}_\alpha-x_\alpha\vec{N}_\beta}{\mathcal{D}^{eff}_{\alpha\beta}}+\frac{\vec{N}_\alpha}{\mathcal{D}^{eff}_{K\alpha}}+\frac{1}{\mathcal{D}^{eff}_{K\alpha}}\frac{p_\alpha}{RT}\frac{B_0}{\mu}\nabla p \tag{9}$$

where $\vec{N}_\alpha$ is the total molar flux of species α, B_0 is a constant porous-medium permeability-coefficient, and $\mathcal{D}^{eff}_{\alpha\beta}=(\varepsilon/\tau)\mathcal{D}_{\alpha\beta}$ and $\mathcal{D}^{eff}_{K\alpha}=(\varepsilon/\tau)\mathcal{D}_{K\alpha}$ stand for the effective binary and Knudsen diffusion coefficients respectively (see Appendices A.2 and A.3).

Considering the total molar flux of species α, $\vec{N}_\alpha = W_\alpha^{-1}(\rho y_\alpha\langle\vec{v}\rangle+\langle\vec{j}_\alpha\rangle)$, Eq. (8) is rewritten as

$$\frac{\partial(\varepsilon c_\alpha)}{\partial t}+\nabla\cdot\vec{N}_\alpha=S_{x\alpha} \tag{10}$$

where $S_{x\alpha}$ is the volumetric molar sources or sinks of species α, $S_{x\alpha}=W_\alpha^{-1}S_{y\alpha}$.

Replacing Eq. (9) into Eq. (10) and rearranging it results in

$$\frac{\partial(\varepsilon c_\alpha)}{\partial t}-\nabla\cdot(\Gamma^*_\alpha\nabla p_\alpha)+\nabla\cdot(\vec{v}^{\,p^*}_\alpha p_\alpha)+\nabla\cdot(\vec{v}^{\,N^*}_\alpha p_\alpha)=S_{x_\alpha} \tag{11}$$

where the following coefficients, here referred to as DGM parameters, have been defined for compactness and ease of interpretation:

$$\Gamma^*_\alpha=\frac{\Gamma_\alpha}{RT}\rightarrow\Gamma_\alpha=\frac{1}{\left[\sum_{\beta\neq\alpha}\left(\frac{p_\beta}{p\mathcal{D}^{eff}_{\alpha\beta}}\right)+\frac{1}{\mathcal{D}^{eff}_{K\alpha}}\right]} \tag{12}$$

$$\vec{v}^{\,p^*}_\alpha=\frac{\vec{v}^{\,p}_\alpha}{RT}\rightarrow\vec{v}^{\,p}_\alpha=\frac{\Gamma_\alpha}{\mathcal{D}^{eff}_{K\alpha}}\left(-\frac{B_0}{\mu}\nabla p\right) \tag{13}$$

$$\vec{v}^{\,N^*}_\alpha=\frac{\vec{v}^{\,N}_\alpha}{RT}\rightarrow\vec{v}^{\,N}_\alpha=\Gamma_\alpha RT\sum_{\beta\neq\alpha}\left(\frac{\vec{N}_\beta}{p\mathcal{D}^{eff}_{\alpha\beta}}\right) \tag{14}$$

Γ_α ($m^2\,s^{-1}$) represents a global diffusion coefficient of species α in the multicomponent gas mixture in a porous media ; $\vec{v}^{\,p}_\alpha$ ($m\,s^{-1}$) is a superficial velocity due to the pressure gradient in the porous medium; and $\vec{v}^{\,N}_\alpha$ ($m\,s^{-1}$) is a superficial velocity induced by the flow of the other species.

Eq. (11), applied to all the components of the gas mixture, represents the complete set of equations for mass transport, and do not need to be supplemented by any additional equations of motion [37]. The global pressure p can be computed as

$$p=\sum_{\forall\alpha}p_\alpha \tag{15}$$

and the superficial permeation velocity may then be estimated using Darcy's Law [40]:

$$\langle\vec{v}\rangle=-\frac{B_0}{\mu}\nabla p \tag{16}$$

The authors have published an open-source species mass transfer library that includes this DGM algorithm, it is available in [41].

The sensible enthalpy conservation equation in a porous medium, assuming local thermal equilibrium between the porous matrix and the fluid flowing through the interstitial space [42], is

$$\frac{\partial[\varepsilon\rho_f h_f+(1-\varepsilon)\rho_s h_s]}{\partial t}+\nabla\cdot(\rho_f h_f\langle\vec{v}\rangle)+\nabla\cdot[\varepsilon\vec{q}_f+(1-\varepsilon)\vec{q}_s]=\omega \tag{17}$$

where the subscripts f and s stand for fluid and solid respectively, and the following assumptions and provisions have been made: the power delivered to the fluid by the body forces and the viscous dissipation are negligible; there are no large pressure differences in the system; and there are no volumetric heat sources within the electrodes because Joule heating takes place only within the electrolyte, and radiation can be neglected in the opaque electrodes [34,33]. Note that surface-to-surface radiative heat flux, $\vec{q}_{rad}$, is considered at the electrode outer boundary by means of a boundary condition (see Section 2.4).

The diffusive heat fluxes appearing in Eq. (17) are given by

$$\vec{q}_f=-\lambda_f\nabla T+\sum_{\forall\alpha}(\vec{j}_\alpha h_\alpha) \tag{18}$$

$$\vec{q}_s=-\lambda_s\nabla T \tag{19}$$

An effective thermal conductivity of the porous medium can be defined as $\lambda^{eff}=\varepsilon\lambda_f+(1-\varepsilon)\lambda_s$ [43]. Considering Eqs. (18), (19) and the following relationship:

$$\rho_f h_f\langle\vec{v}\rangle+\sum_{\forall\alpha}(\langle\vec{j}_\alpha\rangle h_\alpha)=\sum_{\forall\alpha}[h_\alpha(W_\alpha\vec{N}_\alpha)] \tag{20}$$

then Eq. (17) can be rewritten, after some rearrangement, as

$$\begin{aligned}&[\varepsilon\rho_f C_{p,f}+(1-\varepsilon)\rho_s C_{p,s}]\frac{\partial T}{\partial t}+\nabla\cdot\left[T\sum_{\forall\alpha}(C_{p\alpha}W_\alpha\vec{N}_\alpha)\right]-\nabla\cdot(\lambda^{eff}\nabla T)\\&\quad=T\nabla\cdot\left[\sum_{\forall\alpha}(C_{p\alpha}W_\alpha\vec{N}_\alpha)\right]-\sum_{\forall\alpha}[h_\alpha\nabla\cdot(W_\alpha\vec{N}_\alpha)]\\&\quad-\varepsilon h_f\frac{\partial\rho_f}{\partial t}-(1-\varepsilon)h_s\frac{\partial\rho_s}{\partial t}+\omega\end{aligned} \tag{21}$$

where ω, the heat of reaction, has two contributions: (a) due to the reversible reaction heat release (Q_{rev}), this being released only in the fuel electrode; and (b) due to the irreversibilities of the process (Q_{irrev}), this being released where such irreversibilities or overpotentials take place. Thus,

$$\omega=\begin{cases}Q_{irrev,c} & \text{in the air electrode}\\ Q_{rev}+Q_{irrev,a} & \text{in the fuel electrode}\end{cases} \tag{22}$$

The chemical reaction is assumed to take place on the electrode–electrolyte interfaces, and thus this is where the heat of reaction is released; it is therefore accounted for in Eq. (21) as a heat flux boundary condition (see Section 3).

2.3. The electrolyte model

The electrolyte is an impervious solid traversed by an anionic (O^{2-}) flux. The model consists of equations for the conservation of charge, which simultaneously enforces mass conservation, and of energy.

The charge-conservation equation is, considering Ohm's Law, as follows:

$$\frac{\delta\tilde{\rho}}{\delta t}-\nabla\cdot(\tilde{\sigma}_e\nabla\phi_e)=0 \tag{23}$$

where $\tilde{\rho}$ is the volumetric charge density, $\tilde{\sigma}_e$ is the ionic conductivity of the electrolyte (see Appendix A.7), and ϕ_e is the electric potential of the ion-conducting phase of the electrolyte.

Heat transfer in the electrolyte is due to conduction. Considering: (i) Fourier's law, $\vec{q}=-\lambda\nabla T$; (ii) Joule heating, $Q=i^2\tilde{\sigma}_e^{-1}$; and (iii) the definition of sensible enthalpy, $dh=C_p\,dT$, then the energy conservation equation can be written in terms of temperature as

$$\rho C_p\frac{\partial T}{\partial t}-\nabla\cdot(\lambda\nabla T)=-h\frac{\partial\rho}{\partial t}+\frac{i^2}{\tilde{\sigma}_e} \tag{24}$$

where $i=|\vec{i}|$ is the current density magnitude.

For those cell configurations where the electrolyte is exposed to the channels, such as the case of a microtubular cell where the cathode is shorter than the electrolyte, the surface-to-surface radiative heat exchange is included as a heat-flux boundary condition using a surface-to-surface radiation-model (see Section 2.4).

2.4. The radiation model

The importance of radiative heat transfer has been discussed in the SOFC-modelling literature [33,34,14]. The prevailing ideas are: (i) the most common gases in SOFCs behave as non-participating media, and thus surface-to-surface radiation exchange is the only radiative transfer mode that needs to be considered in the

channels of an SOFC; (ii) the electrodes are opaque to radiation; (iii) the effect of volumetric radiation within a thin electrolyte is negligible, though the electrolyte material is optically thin. These conclusions are also applicable to SOEC.

The accurate calculation of surface-to-surface radiation requires of complex models accounting for both parallel and oblique radiation [14], such the view-factor method used in the present work [44]:

$$q_{rad,i} = \xi_i \left\{ E_{b,i} - \sum_j (F_{i-j} E_{b,j}) - H_{o,i} + \sum_j \left[\left(\frac{1}{\xi_j} - 1 \right) F_{i-j} q_{rad,j} \right] \right\} \quad (25)$$

where $q_{rad,i}$ is the surface-to-surface radiative heat flux arriving at the infinitesimal, isothermal surface element dA_i; and j indicates an infinitesimal, isothermal element of surface dA_j irradiating element i. In Eq. (25), ξ is the emissivity of the surface, $E_b = \sigma_{sb} T^4$ is the blackbody emissive power, σ_{sb} being the Stefan–Boltzmann constant; H_o is the incident radiation entering or leaving the domain through an opening (H_o=0, in this work), and F_{i-j} is the view factor between the two infinitesimal elements dA_i and dA_j. The view factors are defined as

$$F_{i-j} = \frac{\cos\ \theta_i \cos\ \theta_j}{\pi r^2} dA_j \quad (26)$$

where θ_i and θ_j are the angles between the normal vector to the surface elements dA_i and dA_j and the line (of length r) connecting them. Further details of the radiation model are given elsewhere [16].

2.5. The electrochemical model

The electrochemical model represents the electrochemical reaction that takes place at the triple phase boundaries (TPBs), where electrolyte, reactants and the catalyst region of the electrode meet. These TPBs are confined to a region close to the electrode–electrolyte interface and therefore the reaction is represented as occurring on a surface.

In the following subsections the electrochemical models for the SOFC and SOEC operating modes are presented.

2.5.1. SOFC mode

The electrochemical reaction that takes place in a hydrogen-fed SOFC is

$$H_2 + \tfrac{1}{2} O_2 \rightarrow H_2O$$

The standard expression for the cell voltage of such a reacting system is

$$V = V_{oc} - \eta_{conc,a} - \eta_{conc,c} - \eta_{ohm} - \eta_{act,a} - \eta_{act,c} \quad (27)$$

where subscripts a and c stand for the fuel and air electrodes respectively (see Table 3) and η_{conc}, η_{ohm}, η_{act} are the concentration, ohmic and activation overpotentials respectively. These overpotentials, which are positive, are defined below:

- Concentration overpotential:

$$\eta_{conc,a} = \frac{RT}{2F} \ln \left(\frac{p_{H_2,b} p_{H_2O,ra}}{p_{H_2O,b} p_{H_2,ra}} \right) \quad (28)$$

$$\eta_{conc,c} = \frac{RT}{2F} \ln \left(\frac{\sqrt{p_{O_2,b}}}{\sqrt{p_{O_2,rc}}} \right) \quad (29)$$

Table 3
Electrochemical roles of the cell electrodes for both operating modes.

Electrode	Label	SOFC mode	SOE mode
Fuel electrode	a	Oxidation	Reduction
Air electrode	c	Reduction	Oxidation

- Ohmic overpotential: From Eq. (27)

$$\eta_{ohm} = V_{oc} - V - \eta_{conc,a} - \eta_{conc,c} - \eta_{act,a} - \eta_{act,c} \quad (30)$$

where by definition [45]

$$\eta_{act,a} = E_a - E_{eq,a} \quad (31)$$

$$\eta_{act,c} = E_{eq,c} - E_c \quad (32)$$

$$V_{oc} = V_{rev} + \eta_{conc,a} + \eta_{conc,c} \quad (33)$$

with $E_{eq,a}$, $E_{eq,c}$, E_a, E_c and V_{rev} being defined as

$$E_{eq,a} = \left[-E^o - \frac{RT}{2F} \ln \left(\frac{p_{H_2,ra}}{p_{H_2O,ra}} \right) \right] \quad (34)$$

$$E_{eq,c} = \frac{RT}{2F} \ln \left[\left(\frac{p_{O_2,rc}}{p_{ref}} \right)^{1/2} \right] \quad (35)$$

$$E_a = \phi_a - \phi_{e,a} \quad (36)$$

$$E_c = \phi_c - \phi_{e,c} \quad (37)$$

$$V_{rev} = E_{eq,c} - E_{eq,a} \quad (38)$$

Here ϕ_a and ϕ_c are the electric potentials of the electron-conducting phase in the fuel and air electrodes; and $\phi_{e,a}$ and $\phi_{e,c}$ are the electric potentials of the ion-conducting phase in the fuel and air electrodes respectively.

From Eqs. (31) to (38), Eq. (30) may be rewritten as

$$\eta_{ohm} = \phi_{e,ra} - \phi_{e,rc} + \phi_{c,rc} - \phi_{a,ra} - V \quad (39)$$

In the present work, the electrodes are assumed to be ideal electron conductors:

$$\nabla \phi_a = 0 \quad \Rightarrow \phi_a = \text{constant} \quad \Rightarrow \phi_{a,ra} = \phi_{a,ia} \quad (40)$$

$$\nabla \phi_c = 0 \quad \Rightarrow \phi_c = \text{constant} \quad \Rightarrow \phi_{c,rc} = \phi_{c,ic} \quad (41)$$

where $\phi_{a,ia}$ and $\phi_{c,ic}$ are the electric potential of the electron-conductor phase of the electrode at the electrode–interconnect interface, that satisfy the following equation:

$$V = \phi_{c,ic} - \phi_{a,ia} \quad (42)$$

Therefore, from Eqs. (40), (41), (42) and (39), the ohmic overvoltage is defined as

$$\eta_{ohm} = \phi_{e,ra} - \phi_{e,rc} \quad (43)$$

The ohmic overpotential is, in Eq. (27), defined as a positive magnitude; therefore from Eq. (43):

$$\eta_{ohm} > 0 \Rightarrow \phi_{e,ra} > \phi_{e,rc} \quad (44)$$

Eq. (44) conflicts with Ohm's law ($\phi_{e,ra} < \phi_{e,rc}$) as the current flows from the cathode to the anode. To remedy this, a new variable is used:

$$\phi_e^* = -\phi_e \quad (45)$$

Eqs. (31) and (32) may be rewritten as

$$\eta_{act,a} = \phi_{a,ra} + \phi^*_{e,ra} - E_{eq,a} \quad (46)$$

$$\eta_{act,c} = E_{eq,c} - \phi_{c,rc} - \phi^*_{e,rc} \quad (47)$$

From Eqs. (30), (46) and (47)

$$\eta_{ohm} = \phi^*_{e,rc} - \phi^*_{e,ra} + \underbrace{\phi_{c,rc} - \phi_{a,ra}}_{V} - V \quad (48)$$

Therefore, the ohmic overpotential is redefined as

$$\eta_{ohm} = \phi^*_{e,rc} - \phi^*_{e,ra} \quad (49)$$

where η_{ohm} is positive as required and ϕ^* satisfies Ohm's law ($\phi^*_{e,ra} < \phi^*_{e,rc}$).

- Activation overpotential:
This is given by the most general form of Butler–Volmer equation [46]:

$$i_{ra} = i_{o,a}\left[\exp\left(\frac{\alpha_{b,a}F\eta_{act,a}}{RT}\right) - \exp\left(-\frac{\alpha_{f,a}F\eta_{act,a}}{RT}\right)\right] \quad (50)$$

$$i_{rc} = i_{o,c}\left[\exp\left(\frac{\alpha_{b,c}F\eta_{act,c}}{RT}\right) - \exp\left(-\frac{\alpha_{f,c}F\eta_{act,c}}{RT}\right)\right] \quad (51)$$

where α_b and α_f are the backward and forward transfer coefficients, and $i_{o,a}$ and $i_{o,c}$ are the exchange current densities at each electrode, for the calculation of which the following experimental correlations are widely used [47,48]:

$$i_{o,a} = \gamma_a\, x^a_{H_2}\, x^b_{H_2O} \exp\left(-\frac{E_{act,a}}{RT}\right) \quad (52)$$

$$i_{o,c} = \gamma_c\, x^c_{O_2} \exp\left(-\frac{E_{act,c}}{RT}\right) \quad (53)$$

with $E_{act,a}$ and $E_{act,c}$ being the anodic and cathodic activation energies; a, b and c expressing the concentration dependency; and γ_a and γ_c being the anodic and cathodic pre-exponential coefficients respectively.

2.5.2. SOEC mode

If the cell operates as an SOEC, the electrochemical reaction is reversed:

$$H_2O \rightarrow H_2 + \tfrac{1}{2}O_2$$

The cell voltage is given by Eq. (27), where the open circuit voltage of the reverse reaction is to be considered: $V_{oc,SOEC} = -V_{oc,SOFC}$. Hence,

$$V = V_{oc,SOEC} - \eta_{conc,a} - \eta_{conc,c} - \eta_{act,a} - \eta_{act,c} - \eta_{ohm} \quad < 0 \quad (54)$$

The overpotentials are positive magnitudes, and their definitions slightly differ from those in the SOFC mode, as indicated below:

- Concentration overpotential:

$$\eta_{conc,a} = \frac{RT}{2F}\ln\left(\frac{p_{H_2O,b}\,p_{H_2,ra}}{p_{H_2,b}\,p_{H_2O,ra}}\right) \quad (55)$$

$$\eta_{conc,c} = \frac{RT}{2F}\ln\left(\frac{\sqrt{p_{O_2,rc}}}{\sqrt{p_{O_2,b}}}\right) \quad (56)$$

- Activation overpotential: $\eta_{act,a}$ and $\eta_{act,c}$ are given by Eqs. (50) and (51) respectively, where $i_{o,a}$ and $i_{o,c}$ are given by Eqs. (52) and (53), since the exchange current density is by definition the same for the direct (SOFC) and reverse (SOEC) reactions; however the charge transfer coefficients change according to

$$\alpha_{b,a,SOEC} = \alpha_{f,a,SOFC} \quad (57)$$

$$\alpha_{b,c,SOEC} = \alpha_{f,c,SOFC} \quad (58)$$

$$\alpha_{f,a,SOEC} = \alpha_{b,a,SOFC} \quad (59)$$

$$\alpha_{f,c,SOEC} = \alpha_{b,c,SOFC} \quad (60)$$

- Ohmic overpotential: η_{ohm} is defined in Eq. (43) as $\eta_{ohm} = \phi_{e,ra} - \phi_{e,rc}$. In an SOEC, the current flows from the fuel electrode to the air electrode and thus

$$\eta_{ohm} > 0 \Rightarrow \phi_{e,ra} > \phi_{e,rc} \Rightarrow \phi^*_e = \phi_e \quad (61)$$

In summary, the electrochemical model consists of a set of algebraic equations, namely Eqs. (27), (28), (29), (49), (50) and (51) for SOFC mode and Eqs. (27), (55), (56), (49), (50) and (51) for SOEC model. However, the transfer coefficients (α_b, α_f) and the exchange current densities ($i_{o,a}, i_{o,c}$) in Eqs. (50) and (51) are cell dependent and not measured experimentally. Hence, for completely specifying a model, these values are often guessed in a data fitting process; in this work, this is presented in Section 5.

3. Numerical details

The numerical solution of the mathematical model introduced in Section 2 has been addressed by developing an in-house algorithm solvable in OpenFOAM-1.5-dev [30] using a finite-volume method. In this work we study the steady-state SORFC operation, and therefore the time derivatives in the transport equations are null.

To facilitate the implementation of the mathematical model, the spatial domain is split into subdomains for each of the five cell components; each subdomain is meshed separately resulting in five conformal adjacent meshes (Fig. 1), namely: (i) `fuelChannelMesh` for the fuel channel domain; (ii) `anodeMesh` for the fuel electrode; (iii) `electrolyteMesh` is the mesh for the electrolyte subdomain; (iv) `cathodeMesh` for the air electrode; and (v) `airChannelMesh` for the air channel. These numerical grids are adjacent to each other; between two adjacent meshes there is only one physical boundary but this is represented twice in the numerical model, one for each of the two adjacent meshes (these are the so-called *coupled boundaries*).

The overall algorithm linking the several solution procedures is embodied in a main code. Its salient algorithmic steps are shown in Fig. 2. First, the computational meshes are created and checked, returning a fatal error if they are not face-matching. Then, the fields required in each spatial domain are created and their values initialised. Next, the radiation model is solved providing the radiative heat fluxes to be introduced as a source term in the energy-conservation equation for the air electrode and the electrolyte [16]. Hence, from Eq. (24) the energy-conservation equation in the electrolyte, considering surface-to-surface radiation and steady state, is

$$-\nabla\cdot(\lambda\nabla T) = \frac{i^2}{\tilde{\sigma}} - \nabla\cdot\vec{q}_{rad} \quad (62)$$

where $\vec{q}_{rad}$ is non-zero only at the radiative boundaries of the electrolyte. Similarly, from Eq. (21) the energy-conservation equation in the air electrode, considering surface-to-surface radiation and steady-state conditions, is

$$\nabla\cdot\left[T\sum_{\forall\alpha}(C_{p\alpha}W_\alpha\vec{N}_\alpha)\right] - \nabla\cdot(\lambda^{eff}\nabla T) = T\nabla\cdot\left[\sum_{\forall\alpha}(C_{p\alpha}W_\alpha\vec{N}_\alpha)\right] - \sum_{\forall\alpha}[h_\alpha\nabla\cdot(W_\alpha\vec{N}_\alpha)] - \nabla\cdot\vec{q}_{rad} \quad (63)$$

where $\vec{q}_{rad}$ is non-zero only at the radiative boundaries of the air electrode.

The electrode model is solved at both electrodes and the relevant information, such as velocity, pressure and species concentrations at the coupled boundaries, is transferred to the adjacent channel sub-domains. Chemical reaction is modelled as a surface reaction; therefore, in Eq. (11) $S_{x_\alpha} = 0$ and the mass source/sink is imposed at the reaction wall as a fixed gradient

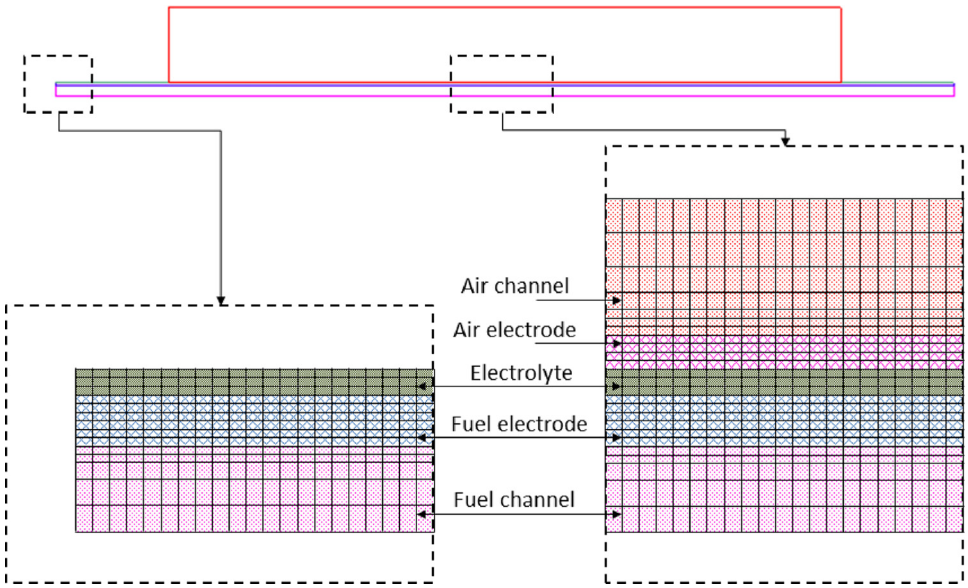


Fig. 1. Schematic of the numerical multi-domain.

```
SORFC-solver
  {
    for(startTime, startTime < endTime, startTime +=deltaTime)
    {
       create: fuelChannelMesh, anodeMesh, electrolyteMesh, cathodeMesh,
               airChannelMesh;
       checkCoupledPatches;
       create: fuelChannelFields, anodeFields, electrolyteFields, cathodeFields,
               airChannelFields;
       fieldsInitialization;

       radiationSolve;

       electrodesSolve;
       electrodeToChannelCoupling;


       channelsSolve;
       channelToElectrodeCoupling;


       electrochemistrySolve;
       electrolyteSolve;

       checkBalances;
       write;
    }
  exit
  }
```

Fig. 2. Structure of the segregated solver for the mathematical model of an SORFC.

boundary condition given by

$$\nabla p_{\alpha,r} = -RT_r\left\{\sum_{\beta\neq\alpha}\left[\frac{x_{\beta,r}\vec{N}_{\alpha,r}-x_{\alpha,r}\vec{N}_{\beta,r}}{\mathcal{D}^{eff}_{\alpha\beta,r}}\right] + \frac{\vec{N}_{\alpha,r}}{\mathcal{D}^{eff}_{K\alpha,r}} + \frac{1}{\mathcal{D}^{eff}_{K\alpha,r}}\frac{p_{\alpha,r}}{RT_r}\frac{B_0}{\mu_r}\nabla p_r\right\} \tag{64}$$

where $\vec{N}_{\alpha,r}$ is given by Faraday's law. Similarly, in Eq. (21) $\omega = 0$ and the reaction heat is introduced as boundary heat fluxes. Thus, from Eq. (63):

$$\nabla\cdot\left[T\sum_{\forall\alpha}(C_{p\alpha}W_\alpha\vec{N}_\alpha)\right] - \nabla\cdot(\lambda^{eff}\nabla T) = T\nabla\cdot\left[\sum_{\forall\alpha}(C_{p\alpha}W_\alpha\vec{N}_\alpha)\right] - \sum_{\forall\alpha}[h_\alpha\nabla\cdot(W_\alpha\vec{N}_\alpha)] - \nabla\cdot\vec{q}_{rad} - \nabla\cdot(\vec{q}_{rev}+\vec{q}_{irrev}) \tag{65}$$

where

$$q_{rev,c} = 0 \tag{66}$$

$$q_{rev,a} = [\Delta H_{r,(T=0K)} + nFV_{oc}]|\vec{N}_{fuel,ra} \cdot \vec{n}_{ra}| \quad (67)$$

$$q_{irrev,c} = -i_{rc}(\eta_{act,c} + \eta_{con,c}) \quad (68)$$

$$q_{irrev,a} = -i_{ra}(\eta_{act,a} + \eta_{con,a}) \quad (69)$$

q_{rev} being non-zero only at the fuel electrode reaction surface, it is exothermic if SOFC and endothermic if SOEC; and q_{irrev} being non-zero at both electrode reaction walls, it is exothermic at both electrodes and for both operation modes (SORFC). These fluxes are defined normal to the reaction surfaces.

Next, the channel model is solved for both the fuel and air channels using the SIMPLE velocity–pressure-coupling algorithm to solve the mass- and momentum-conservation equations. The energy-conservation equation is, at this point, conveniently solved for the entire SORFC domain using a coupled solver. Information is then exchanged at the channel–electrode coupled boundaries.

Finally, the electrochemical model equations are solved to calculate the concentration overpotentials explicitly, and the activation overpotentials implicitly using a Newton–Raphson method. Then, the value of the electric potential in the ion-conducting phase (electrolyte) at the reaction boundaries is calculated as follows:

$$\text{SOFC}: \quad \phi^*_{e,rc} = \frac{RT}{2F}\ln\left[\left(\frac{p_{O_2,rc}}{p_{ref}}\right)^{1/2}\right] - \eta_{act,c} \quad (70)$$

$$\text{SOFC}: \quad \phi^*_{e,ra} = -E^o - \frac{RT}{2F}\ln\left(\frac{p_{H_2,ra}}{p_{H_2O,ra}}\right) + \eta_{act,a} + V \quad (71)$$

$$\text{SOEC}: \quad \phi^*_{e,rc} = -\frac{RT}{2F}\ln\left[\left(\frac{p_{ref}}{p_{O_2,rc}}\right)^{1/2}\right] + \eta_{act,c} \quad (72)$$

$$\text{SOEC}: \quad \phi^*_{e,ra} = -E^o + \frac{RT}{2F}\ln\left[\frac{p_{H_2O,ra}}{p_{H_2,ra}}\right] - \eta_{act,a} - V \quad (73)$$

These values are set as at the corresponding boundaries of the effective electric-potential field in the electrolyte; they are needed for the solution of the charge-transfer conservation equation in the electrolyte model, which is solved next, thus providing the current density distribution in the cell at the preset operating voltage. Mass and heat balances are finally checked to ensure conservation at convergence.

4. Experimental data

The applicability and validity of the model and numerical tool is shown in the following sections by comparing the numerical results with the data measured by Laguna-Bercero et al. [10] for their single, self-supported, hydrogen-fed, microtubular SORFC.

The experimental test rig is sketched in Fig. 3. It consists of a cylindrical furnace, at the centre of which a single microtubular SOFC is placed. The furnace has a metal casing and a ceramic cylindrical wall with heating resistances. The space between both surfaces is filled with a thermally insulating material. The microtubular SOFC is longer than the furnace, so that both ends are kept away from the heated area and economical and simple sealing mechanisms can be used. The air electrode, which is shorter than the electrolyte/fuel–electrode tube, is located in the middle of the heated perimeter to keep the temperature of the cell active area close as possible to the furnace preset one. The relevant features of the experimental test-rig and its operating conditions are summarised in Table 4.

The experimental $\bar{i}$–V curves reported by Laguna-Bercero et al. [10] are plotted in Fig. 4. We will use in this paper their experimental results for the SOEC mode up to 1.2 V since the authors subsequently detected electrolyte degradation for higher voltages [49]. Also, the experimental open circuit voltage for the SOEC at 20% H_2O(≈ 0.87 V) is lower that what it is expected according to the Nernst equation (≈ 0.89 V). Laguna-Bercero et al. confirm[1] that this mismatch is attributable to an inaccurate

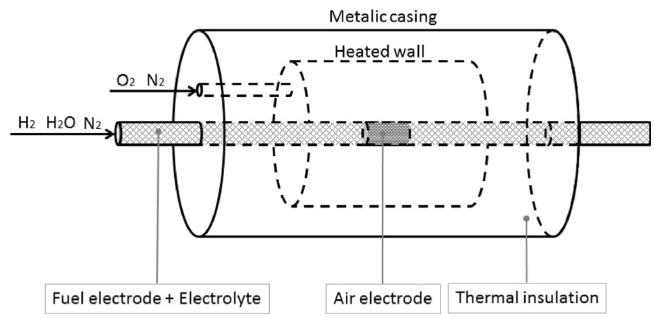


Fig. 3. Schematic of the test rig.

Table 4
Reference microtubular SORFC: geometry and operating conditions.

Microtubular geometry			**SORFC**
Fuel channel internal radius [10]			1.2 mm
Fuel channel length [10]			10 cm
Anode thickness [10]			400 μm
Anode length [10]			10 cm
Anode porosity [54]	ε_a		41.4%
Anode tortuosity factor [64]	τ_a		3
Anode mean pore diameter [54]	$d_{p,a}$		1.2 μm
Anode permeability [64]	$B_{0,a}$		7.65e – 15 m^2
Electrolyte thickness [10]			20 μm
Electrolyte length [10]			10 cm
Cathode thickness [10]			80 μm
Cathode length [10]			1 cm
Cathode porosity [54]	ε_c		37.1%
Cathode tortuosity factor [64]	τ_c		5
Cathode mean pore diameter [54]	$d_{p,c}$		0.12 μm
Cathode permeability[b]	$B_{0,c}$		5.5e – 17 m^2
Air channel external radius[a]			1 cm
Air channel length[b]			7.5 cm
Solid materials properties			**SORFC**
Anode thermal conductivity [65]	$\lambda_{s,a}$		3 W m^{-1} K^{-1}
Electrolyte thermal conductivity [65]	λ_e		2 W m^{-1} K^{-1}
Electrolyte emissivity[a]	ξ_e		0.2
Ionic conductivity constant [65]	A_e		85 000 S m^{-1}
Ionic conductivity constant [65]	B_e		11 000 K
Cathode thermal conductivity [65]	$\lambda_{s,c}$		4 W m^{-1} K^{-1}
Cathode emissivity [66]	ξ_c		0.4
Furnace emissivity[c]	ξ_{oven}		0.8
Reference operating conditions		**SOFC**	**SOEC**
Furnace set temperature [10]	T_{oven}	1168 K	1168 K
Operating pressure [10]	p_{out}	100 000 Pa	100 000 Pa
Fuel temperature at inlet[a]	$T_{in,fuel}$	473 K	473 K
Fuel composition, $H_2 : H_2O : N_2$[10][a]	$x_{\alpha,in,fuel}$	15:70:15	15:70:15
		80:20:0	16:20:64
Fuel flow-rate (at 70%H_2O, T_{room}) [10]	$Q_{in,fuel}$	0.2 l min^{-1}	0.2 l min^{-1}
Fuel flow-rate (at 20%H_2O, T_{room})[a]	$Q_{in,fuel}$	0.125 l min^{-1}	0.125 l min^{-1}
Air composition, $O_2 : N_2$	$x_{\alpha,in}$	0.21:0.79	0.21:0.79
Air flow-rate (at T_{room})[a]	$Q_{in,air}$	0.1 l min^{-1}	0.1 l min^{-1}

[a] Personal communication.
[b] Estimated with the Poiseuille-flow equation [67].
[c] Typical value assumed.

[1] Personal communication.

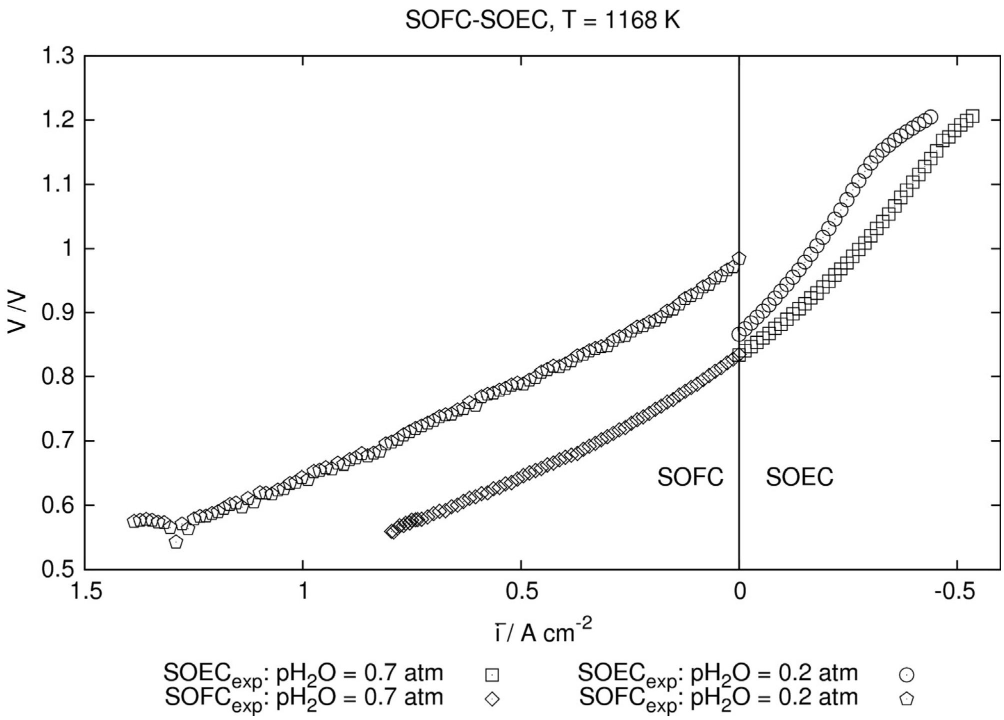


Fig. 4. Experimental characteristic curves of the microtubular SORFC of Laguna-Bercero et al. [10].

performance of the humidifier. The actual composition of the feeding gases has been instead estimated to be 14% H_2, 30% H_2O and 56% N_2. This is therefore the composition used to calculate the numerical curve labelled "$SOEC_{sim}$: $pH_2O = 0.2$ atm".

5. Fitting process

In this section we describe the fitting process employed to assign values to the electrochemical parameters of a particular cell prior to using the model for its simulation.

The need of this fitting process stems from the multiscale nature of the several phenomena in the SORFC. Thus CFD methods usually resolve the macroscale phenomena, while the microscale processes are modelled and included as source terms in the transport equations. This is the case of the electrochemical reaction rate, given by the kinetic equations of Butler–Volmer, Eqs. (50) and (51). These involve the following electrochemical parameters: $\alpha_{\rm b,a}$, $\alpha_{\rm f,a}$, $\alpha_{\rm b,c}$, $\alpha_{\rm f,c}$, $i_{o,a}$, $i_{o,c}$, the values of which are difficult to acquire experimentally.

In the CFD modelling literature, the charge transfer coefficients are often set to 0.5 both for SOFC [15,50,12] and SOEC [17,19,51]. This corresponds to a simple, single-electron-exchange reaction-mechanism [46], despite the fact that hydrogen-oxidation reaction involves 2 electrons. Nevertheless, this simplification is generally accepted because of its ease of use and apparently good results. The present authors did successfully use this assumption in a previous modelling study for SOFCs [16]. However, we find that this value may be inappropriate when modelling the SOFC and SOEC modes simultaneously, as shown below.

The estimation of the exchange current density is typically the other key issue in the parameter fitting process. In the simplest approach among those used in the literature, the exchange current density is assumed constant and its value is fitted, as in [20]. In more comprehensive models, experimental correlations are used to account for the exchange-current-density dependence on temperature and species concentrations. Eqs. (52) and (53) represent typical correlations for the exchange current densities of both electrodes, where γ_a, γ_c are the fitted parameters and the values a, b, c significantly vary from one correlation to another due to their strong dependence on the cell materials and microstructure. None of the CFD models reviewed by the authors using one of these empirical correlations from the literature justify the accuracy of the chosen correlation.

In the following subsections, we present the parameter fitting process performed in this work to estimate the values of the charge-transfer coefficients and the exchange current densities. The aim is to provide more reliable fitted values for SOFC and SOEC that can be used in a quantitative modelling tool.

5.1. Estimation of the charge transfer coefficients

The charge transfer coefficients ($\alpha_{\rm b,a}, \alpha_{\rm f,a}, \alpha_{\rm b,c}, \alpha_{\rm f,c}$) are usually set to 0.5 (*i.e.* single step, single electron transfer) [15,50,12,17,19,51], for the reasons, and despite the shortcomings, referred to above; therefore, for most models the fitted parameters are just the exchange current densities.

Because of our previous successful experience with these values for SOFCs [16], we have in the first instance attempted to use them for the present SOFC-SOEC model. Fig. 5 shows the experimental data of Laguna-Bercero et al. [10] together with the numerical results obtained when taking $\alpha_{\rm b,a} = \alpha_{\rm f,a} = \alpha_{\rm b,c} = \alpha_{\rm f,c} = 0.5$ (see "case-0" in Table 5); the numerical value of $\bar{i}$ is calculated over the air–electrode active area as

$$\bar{i} = \frac{1}{A_{rc}} \int_{A_{rc}} \vec{i}_{rc} \cdot \vec{n}_{rc} \, dA_{rc} \tag{74}$$

From the figure, it is apparent that taking all the charge transfer coefficients as 0.5 seems to work for the SOFC mode (as in [16]) but fails to model the SOEC operation, as indicated by the arrows in magenta. According to the Butler–Volmer equation (Eq. (50)), the magnitude of the current density depends on the forward and backward charge transfer coefficients ($\alpha_{\rm b,a}, \alpha_{\rm f,a}, \alpha_{\rm b,c}, \alpha_{\rm f,c}$) regardless of whether the operating mode is SOFC or SOEC (forward or backward). This is not satisfied by the numerical results shown in Fig. 5. Therefore, in the present study, we reject the hypothesis $\alpha_{\rm b,a} = \alpha_{\rm f,a} = \alpha_{\rm b,c} = \alpha_{\rm f,c} = 0.5$ and we estimate the value of each

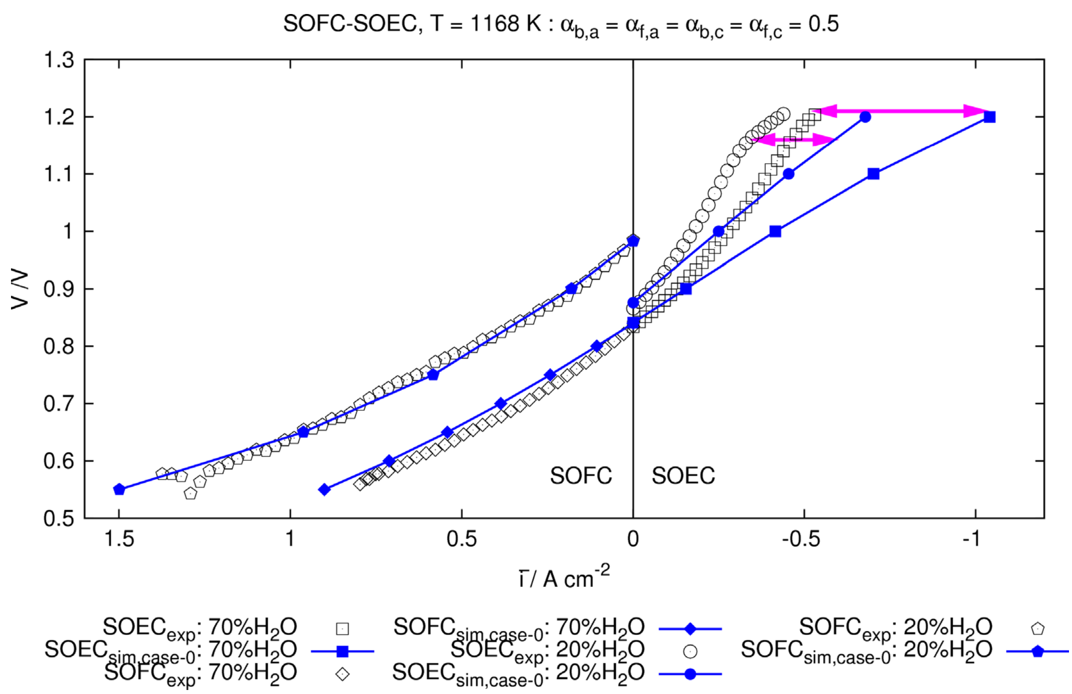


Fig. 5. Characteristic curves of a microtubular SORFC. Experimental data (open symbols) for the cell in Table 4 [10] and simulation results (solid symbols) for different values of $\alpha_{b,a} = \alpha_{f,a} = \alpha_{b,c} = \alpha_{f,c}$ (see Table 5). Arrows highlight discrepancies between measurements and modelling. (For interpretation of the references to color in this figure caption, the reader is referred to the web version of this paper.)

Table 5
Electrochemical parameters for both operating modes and for the different cases studied.

Parameter	SOFC Ref.	SOEC Ref.	SOFC Case-0	SOEC Case-0	SOFC Case-1	SOEC Case-1	SOFC Case-2	SOEC Case-2	SOFC Case-3	SOEC Case-3	SOFC Case-4	SOEC Case-4
$\alpha_{b,a}$	1	0.1	**0.5**	**0.5**	1	0.1	1	0.1	1	0.1	1	0.1
$\alpha_{f,a}$	0.1	1	**0.5**	**0.5**	0.1	1	0.1	1	0.1	1	0.1	1
$E_{act,a}$	120	120	120	120	120	120	120	120	120	120	120	120
γ_a	2.5e9	2.5e9	2.5e9	2.5e9	2.5e9	2.5e9	**1e10**	**1e10**	2.5e9	2.5e9	**5e9**	**5e9**
a	0.11	0.11	0.11	0.11	**1**	**1**	**1**	**1**	**1**	**1**	**1**	**1**
b	0.67	0.67	0.67	0.67	**−0.5**	**−0.5**	**−0.5**	**−0.5**	**−0.5**	**−0.5**	**−0.5**	**−0.5**
c	0.25	0.25	0.25	0.25	0.25	0.25	0.25	0.25	0.25	0.25	0.25	0.25
$\alpha_{b,c}$	0.4	0.1	**0.5**	**0.5**	0.4	0.1	0.4	0.1	0.4	0.1	0.4	0.1
$\alpha_{f,c}$	0.1	0.4	**0.5**	**0.5**	0.1	0.4	0.1	0.4	0.1	0.4	0.1	0.4
$E_{act,c}$	120	120	120	120	120	120	120	120	120	120	120	120
γ_c	2.6e9	2.6e9	2.6e9	2.6e9	2.6e9	2.6e9	2.6e9	2.6e9	**1e10**	**1e10**	**1.8e9**	**1.8e9**

charge transfer coefficient that best fits the experimental data. The resulting values are reported in Table 6; for SOFC mode these are: $\alpha_{b,a} = 1$, $\alpha_{f,a} = 0.1$, $\alpha_{b,c} = 0.4$, $\alpha_{f,c} = 0.1$. For SOEC mode the forward and backward directions are inverted and hence: $\alpha_{b,a} = 0.1$, $\alpha_{f,a} = 1$, $\alpha_{b,c} = 0.1$, $\alpha_{f,c} = 0.4$.

These results may be quantitatively interpreted according to the theory of the Butler–Volmer equation for multistep reactions [46], which states that

$$\alpha_b + \alpha_f = \frac{n}{\nu} \tag{75}$$

with n being the number of electrons exchanged in the electrochemical reaction and ν the number of occurrences of the rate-determining step in the overall reaction. For a hydrogen fed SORFC, such the one studied in this work, $n=2$. Hence, from Eq. (75) $\nu_c = 4$ and $\nu_a = 1.8$, meaning that the limiting step in the air electrode occurs four times and the one in the fuel electrode happens almost twice per each overall reaction.

These values agree qualitatively with those reported by Zhu and Kee [45] (SOFC mode: $\alpha_{b,a} = 1.5$, $\alpha_{f,a} = 0.5$, $\alpha_{b,c} = 0.75$, $\alpha_{f,c} = 0.25$) for a button SOFC with similar materials as those used by Laguna-Bercero et al. [10], *i.e.* Ni-YSZ, YSZ, LSM. Our results also agree with the experimental data of Kawada et al. [23] for a Ni-YSZ SOFC anode (SOFC mode: $\alpha_{b,a} = 2$, $\alpha_{f,a} = 1$) and Kenney and Karan [24] for a LSM/YSZ SOFC cathode ($\alpha_{b,c} = 1.5, \alpha_{f,c} = 0.5$). The agreement is particularly revealing in two respects: (i) the forward

Table 6
Reference microtubular SORFC: electrochemical parameters for both operating modes.

Electrochemical parameters		SOFC	SOEC
Fuel transfer coefficients[a]	$\alpha_{b,a}$, $\alpha_{f,a}$	1, 0.1	0.1, 1
Fuel activation energy [48]	$E_{act,a}$	120 kJ mol^{-1}	120 kJ mol^{-1}
Fuel pre-exponential coefficient[a]	γ_a	2.5e9 A m^{-2}	2.5e9 A m^{-2}
Exponent [47]	a	0.11	0.11
Exponent [47]	b	0.67	0.67
Exponent [48]	c	0.25	0.25
Air transfer coefficients[a]	$\alpha_{b,c}$, $\alpha_{f,c}$	0.4, 0.1	0.1, 0.4
Air activation energy [48]	$E_{act,c}$	120 kJ mol^{-1}	120 kJ mol^{-1}
Air pre-exponential coefficient[a]	γ_c	2.6e9 A m^{-2}	2.6e9 A m^{-2}

[a] Fitted parameters.

charge transfer coefficient is smaller than the backward one for both electrodes; and (ii) the charge transfer coefficients are larger in the fuel electrode than in the air one.

A corollary of this research is that the often-employed assumption $\alpha_{b,a} = \alpha_{f,a} = \alpha_{b,c} = \alpha_{f,c} = 0.5$ fails when properly validated with a complete set of experimental data for the cell operating in direct

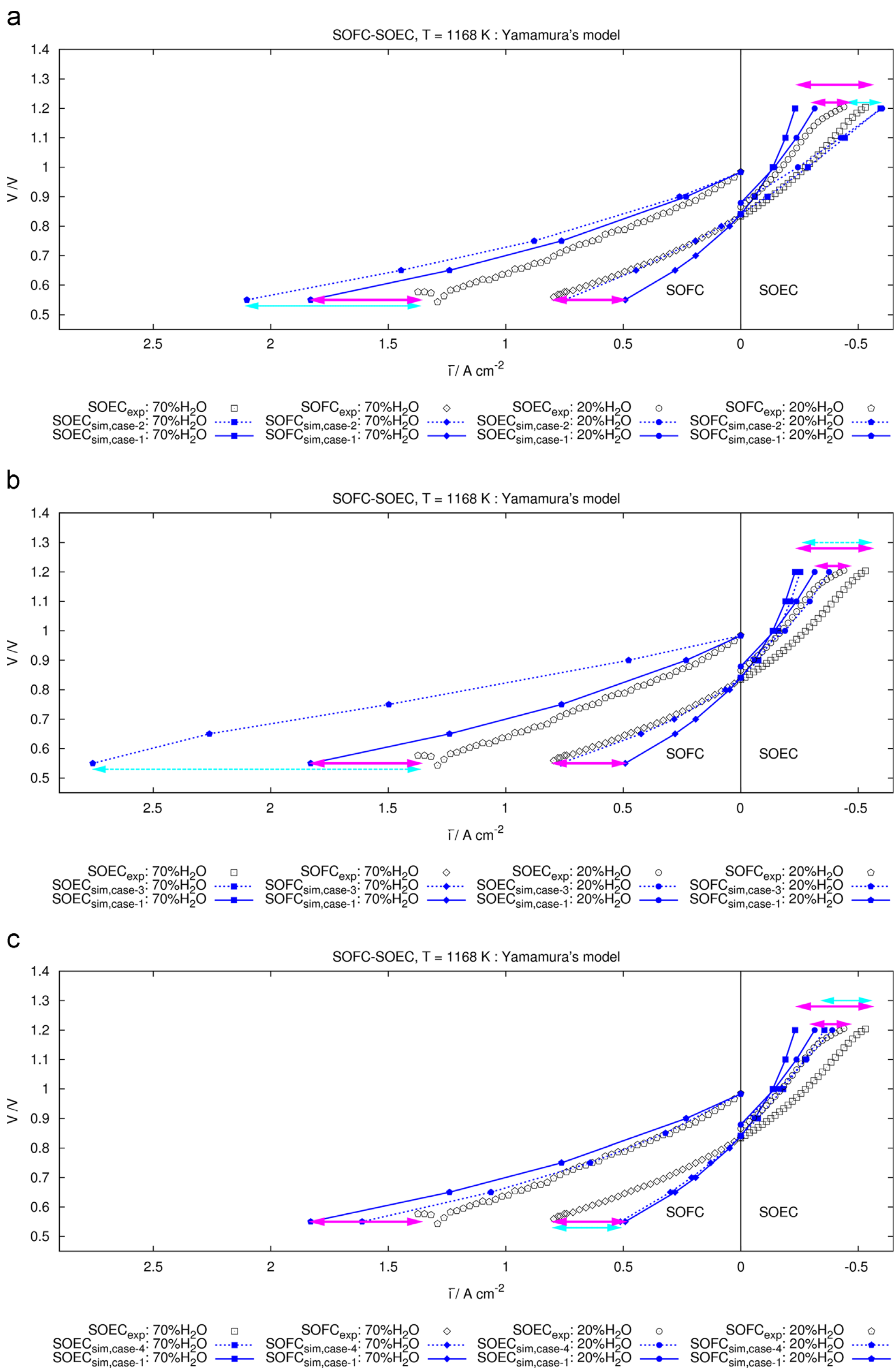


Fig. 6. Characteristic curves of a microtubular SORFC. Experimental data (open symbols) for the cell in Table 4 [10] and simulation results (solid symbols, see Table 5): (a) varying $i_{o,a}$; (b) varying $i_{o,c}$; (c) varying simultaneously $i_{o,a}$ and $i_{o,c}$. (For interpretation of the references to color in this figure caption, the reader is referred to the web version of this paper.)

and reverse mode (SORFC). If the model is only validated with SOFC or SOEC data, the error made by this assumption will be compensated by the data fitting, *i.e.* the exchange current densities, and this in turn can over/under-estimate the activation overpotentials.

5.2. Estimation of the exchange current density

The exchange current density is often estimated using empirical correlations such Eqs. (52) and (53), where a, b, c are set by the correlation and then γ_a, γ_c are the only fitted parameters. In the works reviewed, c is generally set to 0.25 while a and b vary significantly; for instance Yamamura's model specifies $a=1$ and $b=-0.5$ (used in [48,28,52]), Mogensen's model (used in [48,51,17]) chooses $a=b=1$ and recent experimental works report lower values for a and intermediate values for b ($a=0.11$, $b=0.67$) [47,53].

Yamamura's values were used in our previous work [16]. Validation was restricted to a single set of SOFC data, and an acceptable agreement was found. Thus these values were used in a first attempt in the present work to simulate a similar reversible cell for two different fuel compositions. Given $a=1$, $b=-0.5$ (Yamamura) and $c=0.25$, the value of γ_a and γ_c is guessed in a trial and error method aiming at the best possible agreement between numerical and experimental $\bar{i}$–V curves. Representative results from this fitting process are plotted in Fig. 6.

Fig. 6(a) shows the experimental data [10] (open symbols) and two iterations of the fitting process, labelled "case-1" and "case-2" and specified in Table 5. As indicated in the figure by magenta arrows, "case-1" (solid line with symbols) underpredicts the mean current density of the SORFC with 70% H_2O and the SOEC with 20% H_2O; on the contrary, it overpredicts the performance when running the cell as an SOFC with 20% H_2O. In order to get a better fitting, another value of γ_a is assumed in "case-2" (dashed line with symbols). The results of "case-2" improve those of "case-1" reducing the performance underestimation of the latter and providing a good fit for the whole SORFC operating range under conditions of 70% H_2O. However, as it is pointed out with dashed arrows in cyan, "case-2" overpredicts the current density for both SOFC and SOEC operation with 20% H_2O.

Fig. 6(a) shows that when γ_a is modified to improve the fit for curves corresponding to high steam concentrations in the fuel, then the fit of the curves at low steam concentrations worsens.

Similar to Fig. 6(a), Fig. 6(b) shows the results of the fitting process as the value of γ_c is changed; this is increased from "case-1" (solid line with symbols) to "case-3" (dashed line with symbols). It is found that "case-3"(see cyan dashed arrows): (i) provides a good fit for the 70%-H_2O SOFC and the 20%-H_2O SOEC curves; (ii) slightly improves the agreement between the 70%-H_2O SOEC curves; and (iii) worsens the agreement of the 20%-H_2O SOFC curves.

Fig. 6(b) shows that varying the value of γ_c is not enough to get simultaneously a good fit between numerical and experimental data for the four curves considered.

Finally, Fig. 6(c) shows the results when γ_a and γ_c are modified simultaneously. Here "case-4" (dashed line with symbols) is obtained with a lower value of γ_c and a higher value of γ_a than those used in "case-1" (solid line with symbols). The 20%-H_2O SORFC performance is well predicted in "case-4" but it fails in the prediction of the 70 %-H_2O SORFC, as indicated by the dashed cyan arrows.

After several iterations like those represented by "case-1", "case-2", "case-3" and "case-4", we conclude that there is no pair of values for γ_a and γ_c that makes the numerical and experimental data agree simultaneously in all four situations studied. However, some combinations provide a good fit of the SOFC and SOEC curves under the same operating conditions, *e.g.* "case-2" reproduces the performance of the 70 %-H_2O SORFC and "case-4" that of the 20%-H_2O SORFC. Therefore, we conclude that the model can describe the SORFC performance but not its dependence on the fuel concentration. This conclusion points to Yamamura's values as the cause of this underperformance.

The work of Bieberle et al. [53], recently supported by Utz et al. [47], was then used to replace Yamamura's correlation. A fitting process similar to that presented above was conducted using Bieberle's values of $a=0.11$ and $b=0.67$, resulting in a pair of values for γ_a and γ_c that provide good fit of the experimental data both for low and high steam concentrations and in both SOFC and SOEC operations. The best fit is that shown in Fig. 7 for the electrochemical values reported in Table 6.

To summarise this section, we have shown that the results of a macroscale CFD tool strongly depend on the correlation chosen to model the dependence of the exchange current density with the gas

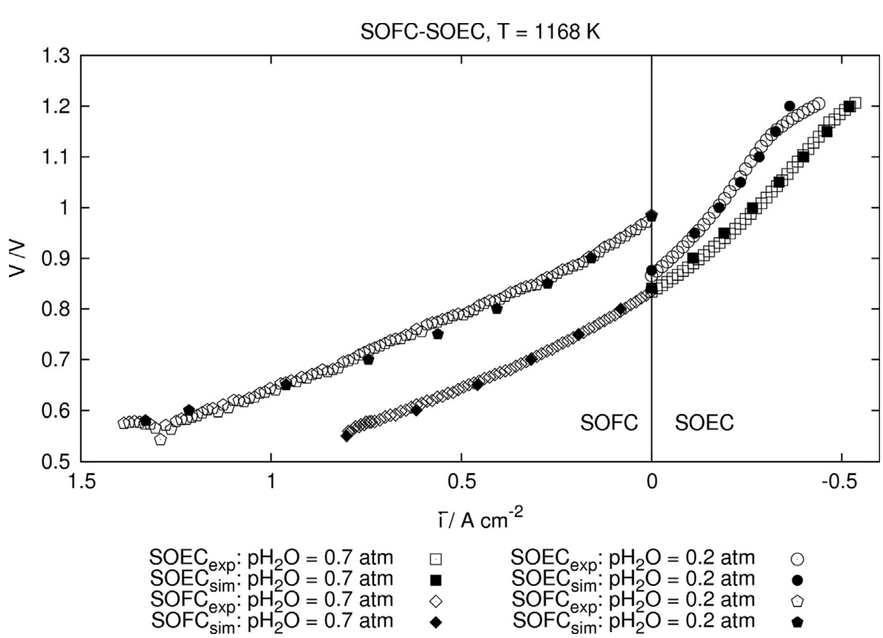


Fig. 7. Characteristic curves of a microtubular SORFC. Experimental data (open symbols) [10] and simulation results (solid symbols) for the cell in Tables 4 and 6.

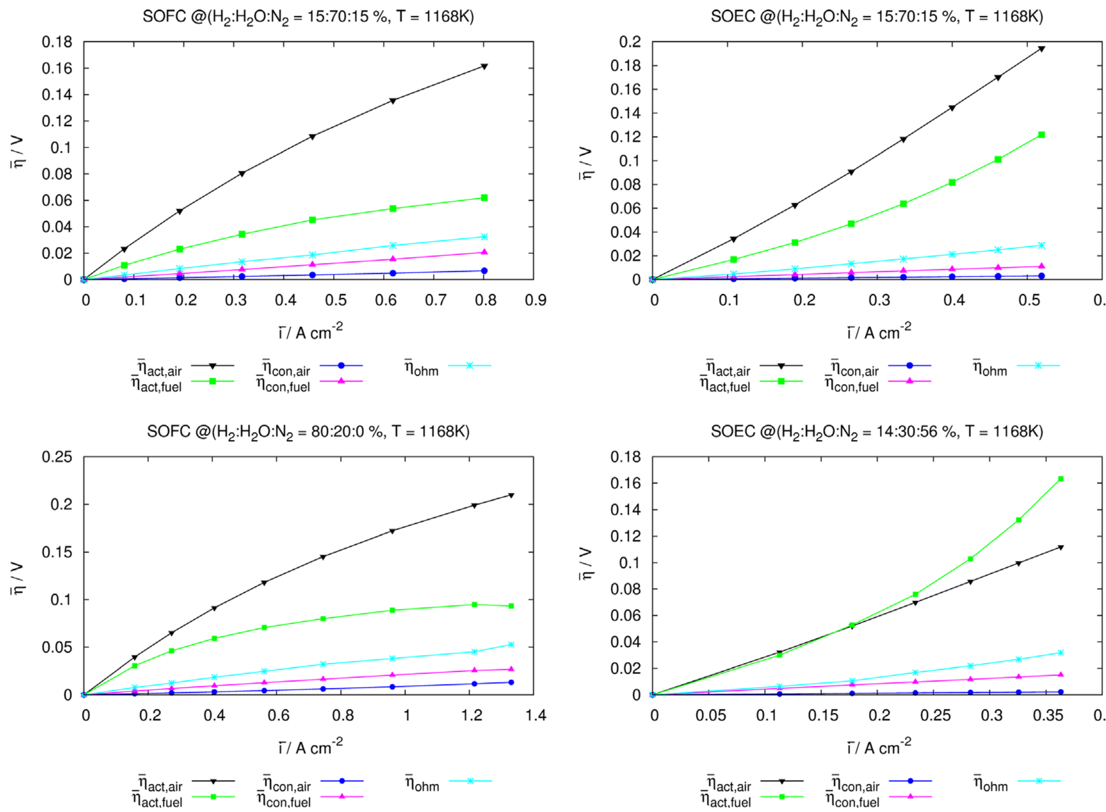


Fig. 8. Mean overpotentials for all the simulations plotted in Fig. 7.

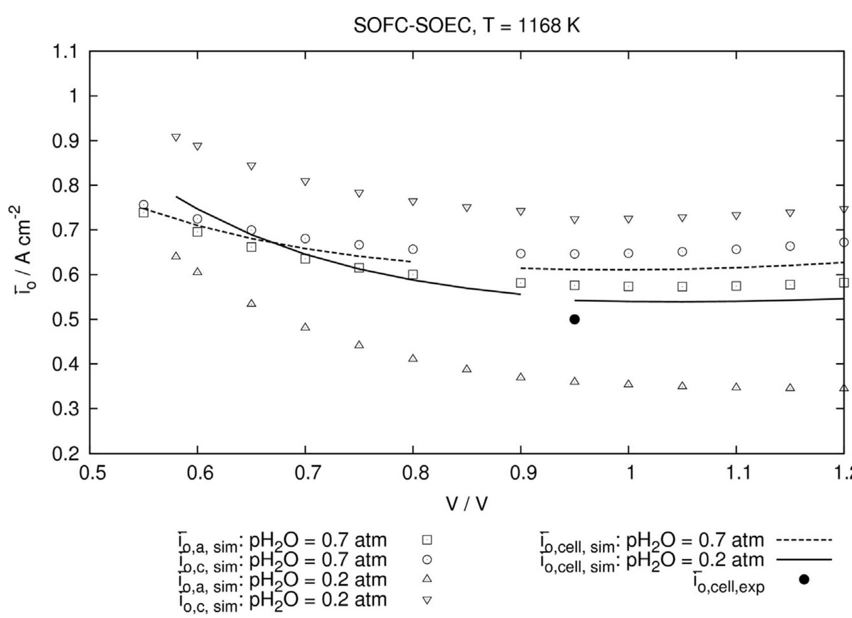


Fig. 9. Mean exchange current density over the electrodes active area for both electrodes ($\bar{i}_{o,a}, \bar{i}_{o,c}$) and for all the simulations plotted in Fig. 7, together with the cell average current exchange density ($\bar{i}_{o,cell} = (\bar{i}_{o,a} + \bar{i}_{o,c})/2$) and a reference experimental value [55].

composition at the microscale. The authors recommend the use of (at least) a couple of experimental data sets with different reactant compositions to check whether a correlation from the literature, expressing this dependence, truly applies to a cell being modelled.

6. Validation

The validation of the mathematical model and numerical tool presented in this work is shown in Fig. 7, where the experimental data for a single, self-supported, hydrogen-fed, microtubular solid oxide regenerative fuel cell [10] is compared with the numerical results obtained after the fitting process presented in the former section. The values of the fitted parameters are reported in Table 6, namely: (i) the pre-exponential coefficients (γ_a, γ_c), the exponents (a, b) in Eq. (52), and the backward and forward transfer coefficients ($\alpha_{b,a}, \alpha_{f,a}, \alpha_{b,c}, \alpha_{f,c}$).

As shown in Fig. 7, numerical and experimental curves are in good agreement. However, the applicability of such numerical tool must be further verified to check the reliability of the values

estimated for the parameters. In the literature, however, this additional validation is rarely performed, probably because of the lack of complementary experimental data to validate against (*e.g.* Electrochemical Impedance Spectroscopy, EIS, analysis).

Fig. 8 shows the distribution of the voltage losses obtained numerically for the given values of the fitted parameters. It is found that the main voltage drop is due to the activation losses, as it may be presumed from experimental data [54,49]. Moreover, Fig. 9 shows the distribution of the calculated mean exchange current densities, which are in the same order of magnitude as the value estimated from experimental EIS data ($\bar{i}_{o,cell} \approx 0.5$ A cm^{-2}) for a similar cell running as SOFC under slightly different operating conditions (V=0.95 V, T=1168 K, H_2: H_2O=4.85:3) [55]. It is thus shown that the values of the fitted parameters not only provide a good accord between the numerical and experimental characteristic curves, but also reliable results of the internal physics of the cell.

7. Conclusions

In this work, we have presented a comprehensive numerical tool for the simulation of a solid oxide regenerative fuel cell. The tool models the following SORFC phenomena: (a) mass transport through channels and porous solids; (b) momentum transport through channels and porous solids; (c) species transfer through channels and porous media (convection, ordinary diffusion, Knudsen diffusion); (d) heat transfer in gases and solids by conduction, convection and surface-to-surface radiation; (e) charge transport through an impervious solid; and (f) reversible electrochemistry.

The validation of such numerical tool involves the fitting of the unknown parameters in the electrochemical model, namely: (i) the pre-exponential coefficients (γ_a, γ_c), the exponents (a, b) in Eq. (52), and the backward and forward transfer coefficients ($\alpha_{b,a}, \alpha_{f,a}, \alpha_{b,c}, \alpha_{f,c}$).

A literature review regarding this fitting process is also presented. It leads to the conclusion that this process often overlooked in the literature, where it is (if at all mentioned) not clearly explained or sufficiently justified. Thus, the fitting is here described in detail. Two corollaries emerges in this research.

First, the often-employed assumption $\alpha_{b,a} = \alpha_{f,a} = \alpha_{b,c} = \alpha_{f,c} = 0.5$ fails when properly validated with a complete set of experimental data for the cell operating in direct and reverse mode (SORFC). Our results suggest that the forward charge transfer coefficient is smaller than the backward one for both electrodes; and that the charge transfer coefficients are larger in the fuel electrode than in the air one.

Second, the relevance of exchange-current-density modelling is also highlighted in this study; we have shown that an accurate modelling of the dependence of the exchange current density on the reactant concentration is paramount for a reliable prediction of the overall cell performance.

The validity of the numerical results provided after the fitting process for some of the uncertain parameters has been shown by comparison with experimental data for an anode-supported microtubular SORFC. Good agreement is found not only between the numerical and experimental $\bar{i}$–V curves, but also between numerical and experimental electrochemical parameters, such as activation overpotentials and exchange current densities, which supports the accuracy of the fitted values.

Acknowledgements

This work is supported by the Science and Innovation Ministry of the Spanish Government (*Ministerio de Ciencia e Innovación, Gobierno de España*) under Project ENE2008-06683-C03-03/CON and CSD2010-00011. The authors are grateful to Prof Orera and Dr. Laguna-Bercero, University of Zaragoza, for many fruitful discussions.

Appendix A. Thermophysical properties

A.1. Viscosity, μ

The semi-empirical formula of Wilke is used to estimate the viscosity of a multicomponent fluid [68]:

$$\mu = \sum_{\forall \alpha} \left[\frac{x_\alpha \mu_\alpha}{\sum_{\forall \beta} (x_\beta \Phi_{\alpha\beta})} \right] \tag{A.1}$$

where

$$\Phi_{\alpha\beta} = \frac{[1 + (\mu_\alpha/\mu_\beta)^{1/2} (W_\beta/W_\alpha)^{1/4}]^2}{(8 + 8W_\alpha/W_\beta)^{1/2}} \tag{A.2}$$

The Sutherland model accounts for the temperature dependence of the viscosity μ_α of each species α:

$$\mu_\alpha = \mu_{o\alpha} \frac{T_{o\mu\alpha} + S_{\mu\alpha}}{T + S_{\mu\alpha}} \left(\frac{T}{T_{o\mu\alpha}} \right)^{3/2} \tag{A.3}$$

where the Sutherland-law parameters ($\mu_o, T_{o\mu}, S_\mu$) are tabulated for the most common gases in [68].

A.2. Binary diffusion coefficient, $D_{\alpha\beta}$

The binary-diffusion coefficients are modelled according to the empirical correlation given by Wilke [69]:

$$D_{\alpha\beta} = 2.628 \times 10^{-3} \frac{\sqrt{T^3 \frac{W_\alpha + W_\beta}{2W_\alpha W_\beta}}}{\sigma^2_{\alpha\beta} \Omega_D p} \tag{A.4}$$

where the binary diffusion coefficient $\mathcal{D}_{\alpha\beta}$ is given in square centimetres per second; the temperature, T, in Kelvin; the molecular weight of species α, W_α, in kilogram per kilomole; the pressure, p, in atmospheres. The average collision diameter, in angstroms, is calculated as

$$\sigma_{\alpha\beta} = \frac{\sigma_\alpha + \sigma_\beta}{2} \tag{A.5}$$

where the value of σ_α (or σ_β) is tabulated for the most common species in [70]. Ω_D is the dimensionless collision integral in the Lennard-Jones 12-6 potential model:

$$\Omega_D = \frac{1.06036}{\mathbb{T}^{0.15610}} + \frac{0.19300}{e^{(0.47635\mathbb{T})}} + \frac{1.03587}{e^{(1.52996\mathbb{T})}} + \frac{1.76474}{e^{(3.89411\mathbb{T})}} \tag{A.6}$$

Here,

$$\mathbb{T} = \frac{Tk_B}{\sqrt{\varepsilon_\alpha \varepsilon_\beta}} \tag{A.7}$$

where k_B is the Boltzmann constant and ε_α is the characteristic Lennard-Jones energy of species α. For the most common gases the value of ε_α is tabulated in [70].

To convert the units of the binary diffusion coefficient and the pressure into the SI system (m^2 s^{-1}, Pa), Eq. (A.4) is modified as follows:

$$D_{\alpha\beta} = 10.1325 \frac{2.628 \times 10^{-3} \sqrt{T^3 \frac{W_\alpha + W_\beta}{2W_\alpha W_\beta}}}{\sigma^2_{\alpha\beta} \Omega_D p} \tag{A.8}$$

where $\sigma_{\alpha\beta}$ is the only parameter that is not expressed in SI system units, as it remains in angstroms.

The diffusion coefficient of a species α in a multicomponent mixture can be calculated as

$$\mathcal{D}_{\alpha m} = \frac{1 - x_\alpha}{\sum_{\beta \neq \alpha} \left(\frac{x_\beta}{\mathcal{D}_{\alpha\beta}} \right)} \tag{A.9}$$

x_α being the molar fraction of species α and $\mathcal{D}_{\alpha\beta}$ being the binary diffusion coefficient defined above.

A.3. Knudsen diffusion coefficient, $D_{K\alpha}$

The Kinetic Theory of Gases defines the Knudsen diffusion coefficient as [71,72]

$$\mathcal{D}_{K_\alpha} = \frac{d_p}{3} \sqrt{\frac{8RT}{\pi W_\alpha}} \tag{A.10}$$

where $\mathcal{D}_{K_\alpha}$ is given in SI units if the temperature is expressed in Kelvin, the molecular weight in kilograms per kilomole, the mean pore diameter (d_p) in meters and the ideal gas law constant in Joule per kilomole per Kelvin.

A.4. Thermal conductivity, λ

Similar to viscosity (Section A.1), the thermal conductivity of the fluid is given by Wilke's formula [68]:

$$\lambda = \sum_{\forall \alpha} \left[\frac{x_\alpha \lambda_\alpha}{\sum_{\forall \beta} (x_\beta \Phi_{\alpha\beta})} \right] \tag{A.11}$$

where

$$\Phi_{\alpha\beta} = \frac{[1 + (\lambda_\alpha/\lambda_\beta)^{1/2} (W_\beta/W_\alpha)^{1/4}]^2}{(8 + 8W_\alpha/W_\beta)^{1/2}} \tag{A.12}$$

The thermal conductivity of each species α, λ_α, is then given by the Sutherland model:

$$\lambda_\alpha = \lambda_{0\alpha} \frac{T_{o\lambda\alpha} + S_{\lambda\alpha}}{T + S_{\lambda\alpha}} \left(\frac{T}{T_{o\lambda\alpha}} \right)^{3/2} \tag{A.13}$$

where the Sutherland-law parameters $(\lambda_o, T_{o\lambda}, S_\lambda)$ are tabulated for the most common gases in [68].

A.5. Specific heat at constant pressure, C_p

The specific heat at constant pressure of a multicomponent gas is calculated as

$$C_p = \sum_{\forall \alpha} y_\alpha C_{p\alpha} \tag{A.14}$$

where $C_{p\alpha}$, the specific heat at constant pressure of species α, is provided by the JANAF thermochemical tables:

$$C_{p\alpha} = \frac{R}{W_\alpha} (a_{1\alpha} + a_{2\alpha} T + a_{3\alpha} T^2 + a_{4\alpha} T^3 + a_{5\alpha} T^4) \tag{A.15}$$

The parameters $a_{1\alpha}, a_{2\alpha}, a_{3\alpha}, a_{4\alpha}, a_{5\alpha}$ are the JANAF constants [73].

A.6. Sensible enthalpy, h

The sensible enthalpy of a multicomponent fluid is given by

$$h = \sum_{\forall \alpha} (y_\alpha h_\alpha) \tag{A.16}$$

where h_α is the sensible enthalpy of each component:

$$h_\alpha = \int_{T_{ref}}^{T} C_{p\alpha} \, dT \tag{A.17}$$

The reference temperature is for convenience set to zero, $T_{ref} = 0$ K. Hence, from Eqs. (A.17) and (A.15):

$$h_\alpha = \frac{R}{W_\alpha} \left(a_{1\alpha} T + \frac{a_{2\alpha}}{2} T^2 + \frac{a_{3\alpha}}{3} T^3 + \frac{a_{4\alpha}}{4} T^4 + \frac{a_{5\alpha}}{5} T^5 \right) \tag{A.18}$$

A.7. Ionic conductivity, $\tilde{\sigma}$

The electrode is the only ion-conductor SOFC-component. Theory and experiments suggest for ion-conducting electrolyte-materials the following equation for the ionic conductivity:

$$\tilde{\sigma}_e = A_e exp\left(\frac{-B_e}{T} \right) \tag{A.19}$$

where the constants A_e and B_e are tabulated for most common SOFC electrolytes in [65].

References

[1] Wang K, Hissle D, Péra MC, Steiner N, Marra N, Sorrentino M, et al. A review on solid oxide fuel cell models. Int J Hydrogen Energy 2011;36:7212–28.

[2] Hajimolana SA, Hussain MA, Daud WMAW, Soroush M, Shamiri A. Mathematical modeling of solid oxide fuel cells: a review. Renew Sustain Energy Rev 2011;15:1893–917.

[3] Erdle E, Dönitz W, Schamm R, Koch A. Reversibility and polarization behaviour of high temperature solid oxide electrochemical cells. Int J Hydrogen Energy 1992;7(10):817–9.

[4] Kusunoki D, Kikuoka Y, Yanagi V, Kugimiya K, Yoshino M, Tokura M, et al. Development of Mitsubishi-planar reversible cell – fundamental test on hydrogen-utilized electric power storage system. Int J Hydrogen Energy 1995;20(10):831–4.

[5] Eguchi K, Hatagishi T, Arai H. Power generation and steam electrolysis characteristics of an electrochemical cell with a zirconia- or ceria-based electrolyte. Solid State Ion 1996;8688(Part 2 (0)):1245–9.

[6] Jensen SH, Sun X, Ebbesen SD, Knibbe R, Mogensen M. Hydrogen and synthetic fuel production using pressurized solid oxide electrolysis cells. Int J Hydrogen Energy 2010;35(18):9544–9.

[7] Tao G, Butler B, Virkar A. Hydrogen and power by fuel-assisted electrolysis using solid oxide fuel cells. ECS Trans 2011;35(1):2929–39.

[8] Marina OA, Pederson LR, Williams MC, Coffey GW, Meinhardt KD, Nguyen CD, et al. Electrode performance in reversible solid oxide fuel cells. J Electrochem Soc 2007;154(5):B452–9.

[9] Hashimoto S, Liu Y, Mori M, Funahashi Y, Fujishiro Y. Study of steam electrolysis using a microtubular ceramic reactor. Int J Hydrogen Energy 2009;34(3):1159–65.

[10] Laguna-Bercero MA, Campana R, Larrea A, Kilner JA, Orera VM. Steam electrolysis using a microtubular solid oxide fuel cell. J Electrochem Soc 2010;157(6):B852–5.

[11] Selimovic A, Kemm M, Torisson T, Assadi M. Steady state and transient thermal stress analysis in planar solid oxide fuel cells. J Power Sources 2005;145: 463–469.

[12] Qu Z, Aravind P, Boksteen S, Dekker N, Janssen A, Woudstra N, et al. Three-dimensional computational fluid dynamics modeling of anode-supported planar SOFC. Int J Hydrogen Energy 2011;34:10209–20.

[13] Danilov VA, Tade MO. A CFD-based model of a planar SOFC for anode flow field design. Int J Hydrogen Energy 2009;34:8998–9006.

[14] Sánchez D, Mun˜oz A, Sánchez T. An assessment on convective and radiative heat transfer modelling in tubular solid oxide fuel cells. J Power Sources 2007;169(1):25–34.

[15] Serincan MF, Pasaogullari U, Sammes NM. Effects of operating conditions on the performance of a micro-tubular solid oxide fuel cell (SOFC). J Power Sources 2009;192(2):414–22.

[16] García-Camprubí M, Jasak H, Fueyo N. CFD analysis of cooling effects in H_2-fed solid oxide fuel cells. J Power Sources 2011;196(17):7290–301.

[17] Ni M, Leung MK, Leung DY. Parametric study of solid oxide steam electrolyzer for hydrogen production. Int J Hydrogen Energy 2007;32(13):2305–13.

[18] Herring JS, O'Brien JE, Stoots CM, Hawkes G, Hartvigsen JJ, Shahnam M. Progress in high-temperature electrolysis for hydrogen production using planar sofc technology. Int J Hydrogen Energy 2007;32(4):440–50.

[19] Grondin D, Deseure J, Ozil P, Chabriat JP, Grondin-Perez B, Brisse A. Computing approach of cathodic process within solid oxide electrolysis cell: experiments and continuum model validation. J Power Sources 2011;196(22):9561–7.

[20] Jin X, Xue X. Mathematical modeling analysis of regenerative solid oxide fuel cells in switching mode conditions. J Power Sources 2010;195(19):6652–8.

[21] Ni M, Leung MK, Leung DY. A modeling study on concentration overpotentials of a reversible solid oxide fuel cell. J Power Sources 2006;163(1):460–6 (special issue including selected papers presented at the second international conference on polymer batteries and fuel cells together with regular papers).

[22] Ni M, Leung MK, Leung DY. Theoretical analysis of reversible solid oxide fuel cell based on proton-conducting electrolyte. J Power Sources 2008;177(2): 369–75.
[23] Kawada T, Sakai N, Yokokawa H, Dokiya M, Mori M, Iwata T. Characteristics of slurry coated nickel zirconia cermet anodes for solid oxide fuel cells. J Electrochem Soc 1990;137(10):3042–7.
[24] Kenney B, Karan K. Mathematical micro-model of a solid oxide fuel cell composite cathode. In: Proceedings – hydrogen and fuel cells 2004, 2004.
[25] Aguiar P, Adjiman C, Brandon N. Anode-supported intermediate temperature direct internal reforming solid oxide fuel cell. i: model-based steady-state performance. J Power Sources 2004;138(12):120–36.
[26] Ni M. Modeling of a solid oxide electrolysis cell for carbon dioxide electrolysis. Chem Eng J 2010;164(15):246–54.
[27] Momma A, Kato T, Kaga Y, Nagata S. Polarization behavior of high temperature solid oxide electrolysis cells (soec). Nippon Seramikkusu Kyokai 1997;105(5): 369–73.
[28] Akhtar N, Decent S, Kendall K. Numerical modelling of methane-powered micro-tubular, single-chamber solid oxide fuel cell. J Power Sources 2010;195(23): 7818–24.
[29] Xie Y, Xue X. Modeling of solid oxide electrolysis cell for syngas generation with detailed surface chemistry. Solid State Ion 2012;224(0):64–73.
[30] The OpenFOAM®-Extended Project. 2011. URL: ⟨http://www.extend-project.de/⟩.
[31] García-Camprubí, M. Multiphysics models for the simulation of solid oxide fuel cells [Ph.D. thesis]. University of Zaragoza; 2011.
[32] Désilets M, Proulx P, Soucy G. Modeling of multicomponent diffusion in high temperature flows. Int J Heat Mass Transf 1997;40(18):4273–8.
[33] Damm DL, Fedorov AG. Radiation heat transfer in SOFC materials and components. J Power Sources 2005;143(1–2):158–65.
[34] Daun KJ, Beale SB, Liu F, Smallwood GJ. Radiation heat transfer in planar SOFC electrolytes. J Power Sources 2006;157(1):302–10.
[35] Krishna R, Wesselingh JA. The Maxwell–Stefan approach to mass transfer. Chem Eng Sci 1997;52(6):861–911.
[36] Suwanwarangkul R, Croiset E, Fowler MW, Douglas PL, Entchev E, Douglas MA. Performance comparison of Fick's, dusty-gas and Stefan–Maxwell models to predict the concentration overpotential of a SOFC anode. J Power Sources 2003;122(1):9–18.
[37] Mason E, Malinauskas A. Gas transport in porous media: the dusty-gas model. New York: Elsevier; 1983.
[38] Kerkhof PJAM. A modified Maxwell–Stefan model for transport through inert membranes: the binary friction model. Chem Eng J Biochem Eng J 1996;64(3): 319–43.
[39] Kerkhof PJ, Geboers MA. Analysis and extension of the theory of multi-component fluid diffusion. Chem Eng Sci 2005;60(12):3129–67.
[40] Nield D, Bejan A. Convection in porous media. 3rd ed. New York: Springer; 2006.
[41] Novaresio V, Garca-Camprub M, Izquierdo S, Asinari P, Fueyo N. An open-source library for the numerical modeling of mass-transfer in solid oxide fuel cells. Comput Phys Commun 2012;183(1):125–46.
[42] Damm DL, Fedorov AG. Local thermal non-equilibrium effects in porous electrodes of the hydrogen-fueled SOFC. J Power Sources 2006;159(2):1153–7.
[43] Tong F, Robert W, Zimmerman LJ. An effective thermal conductivity model of geological porous media for coupled thermo-hydro-mechanical systems with multiphase flow. Int J Rock Mech Min Sci 2009;46:1358–69.
[44] Modest M. Radiative heat transfer. 2nd ed.. Amsterdam: Academic Press; 2003.
[45] Zhu H, Kee RJ. Modeling distributed charge-transfer processes in SOFC membrane electrode assemblies. J Electrochem Soc 2008;155(7):B715–29.
[46] Bockris J, Reddy A. Modern electrochemistry. New York: Plenum Publishing Corporation; 1977.
[47] Utz A, Stormer H, Leonide A, Weber A, Ivers-Tiffee E. Degradation and relaxation effects of ni patterned anodes in H_2–H_2O atmosphere. J Electrochem Soc 2010;157(6):B920–30.
[48] Costamagna P, Honegger K. Modeling of solid oxide heat exchanger integrated stacks and simulation at high fuel utilization. J Electrochem Soc 1998;145(11): 3995–4007.
[49] Laguna-Bercero M, Campana R, Larrea A, Kilner J, Orera V. Electrolyte degradation in anode supported microtubular yttria stabilized zirconia-based solid oxide steam electrolysis cells at high voltages of operation. J Power Sources 2011;196(21):8942–7.
[50] Wang G, Yang Y, Zhang H, Xia W. 3-D model of thermo-fluid and electro-chemical for planar SOFC. J Power Sources 2007;167:398–405.
[51] Laurencin J, Kane D, Delette G, Deseure J, Lefebvre-Joud F. Modelling of solid oxide steam electrolyser: impact of the operating conditions on hydrogen production. J Power Sources 2011;196(4):2080–93.
[52] Andreassi L, Rubeo G, Ubertini S, Lunghi P, Bove R. Experimental and numerical analysis of a radial flow solid oxide fuel cell. Int J Hydrogen Energy 2007;32(17):4559–74.
[53] Bieberle A, Meier LP, Gauckler LJ. The electrochemistry of ni pattern anodes used as solid oxide fuel cell model electrodes. J Electrochem Soc 2001;148(6):A646–56.
[54] Laguna-Bercero MA, Campana R, Larrea A, Kilner JA, Orera VM. Performance and aging of microtubular YSZ-based solid oxide regenerative fuel cells. Fuel Cells 2011;11(1):116–23.
[55] Campana R. Pilas de Combustible de Óxido Sólido Microtubulares y Regenerativas en base YSZ o ScSZ de soporte anódico [Ph.D. thesis]. University of Zaragoza; 2010.
[56] Horita T, Yamaji K, Sakai N, Yokokawa H, Webera A, Ivers-Tiffe E. Electrode reaction of $La_{1-x}Sr_xCoO_{3-d}$ cathodes on $La_{0.8}Sr_{0.2}Ga_{0.8}Mg_{0.2}O_{3-y}$ electrolyte in solid oxide fuel cells. J Electrochem Soc 2001;148(5):A456–62.
[57] Chan SH, Khor KA, Xia ZT. A complete polarization model of a solid oxide fuel cell and its sensitivity to the change of cell component thickness. J Power Sources 2001;93(1–2):130–40.
[58] Huang K, Feng M, Goodenough JB, Milliken C. Electrode performance test on single ceramic fuel cells using as electrolyte sr and mgdoped lagao3. J Electrochem Soc 1997;144(10):3620–4, http://dx.doi.org/10.1149/1.1838058.
[59] Ni M, Leung DY, Leung MK. Electrochemical modeling and parametric study of methane fed solid oxide fuel cells. Energy Convers Manag 2009;50(2):268–78.
[60] Serincan MF, Pasaogullari U, Sammes NM. Computational thermal-fluid analysis of a microtubular solid oxide fuel cell. J Electrochem Soc 2008;155(11): B1117–27.
[61] Udagawa J, Aguiar P, Brandon N. Hydrogen production through steam electrolysis: model-based steady state performance of a cathode-supported intermediate temperature solid oxide electrolysis cell. J Power Sources 2007;166(1):127–36.
[62] Udagawa J, Aguiar P, Brandon N. Hydrogen production through steam electrolysis: model-based dynamic behaviour of a cathode-supported intermediate temperature solid oxide electrolysis cell. J Power Sources 2008;180(1): 46–55.
[63] Hawkes G, O'Brien J, Stoots C, Hawkes B. 3D CFD model of a multi-cell high-temperature electrolysis stack. Int J Hydrogen Energy 2009;34(9):4189–97.
[64] Campana R, Larrea A, Merino R, Villarreal I, Orera VM. SOFC mini-tubulares basadas en YSZ. Boletín Sociedad Espa nola Cerámica y Vidrio 2008;47(4): 189–95.
[65] Bossel UG. Final report on SOFC data: facts & figures. Berne: International Energy Agency, Swiss Federal Office of Energy, Operating Agent Task II; 1992.
[66] Klein JM, Bultel Y, Georges S, Pons M. Modeling of a SOFC fuelled by methane: from direct internal reforming to gradual internal reforming. Chem Eng Sci 2007;62:1636–49.
[67] Jackson R. Transport in porous catalysts. Amsterdam: Elsevier; 1977.
[68] White FM. Viscous fluid flow. New York: McGraw-Hill; 1991.
[69] Wilke CR. Diffusional properties of multicomponent gases. Chem Eng Prog 1950;46:95–104.
[70] Hirschfelder JO, Curtiss CF, Bird RB. Molecular theory of gases and liquids. New York: John Wiley and Sons; 1967.
[71] Welty JR, Wicks CE, Wilson RE, Rorrer G. Fundamentals of momentum, heat and mass transfer. 4th ed.. New York: John Wiley & Sons, Inc.; 2001.
[72] Chapman S, Cowling T. The mathematical theory of non-uniform gases. 3rd ed. Cambridge: Cambridge University Press; 1970.
[73] National institute of standards and technology (NIST). URL: ⟨www.nist.gov⟩ (accessed 17 February 2014).